

Solar Thermochemical Fuel Production: A Novel, Validated Multiphysics Reactor Model for the Reduction–Oxidation of Nonstoichiometric Redox Cycles

Original

Solar Thermochemical Fuel Production: A Novel, Validated Multiphysics Reactor Model for the Reduction–Oxidation of Nonstoichiometric Redox Cycles / Orsini, F., Ferrero, D., Papurello, D., Santarelli, M.. - In: ENERGIES. - ISSN 1996-1073. - ELETTRONICO. - 18:2(2025), pp. 1-36. [10.3390/en18020414]

Availability:

This version is available at: 11583/2996730 since: 2025-01-21T12:14:30Z

Publisher:

mdpi

Published

DOI:10.3390/en18020414

Terms of use:

This article is made available under terms and conditions as specified in the corresponding bibliographic description in the repository

Publisher copyright

(Article begins on next page)

Article

Solar Thermochemical Fuel Production: A Novel, Validated Multiphysics Reactor Model for the Reduction–Oxidation of Nonstoichiometric Redox Cycles

Francesco Orsini ¹, Domenico Ferrero ¹, Davide Papurello ^{1,2,*} and Massimo Santarelli ¹

¹ Department of Energy, Politecnico di Torino, Corso Duca degli Abruzzi 24, 10129 Turin, Italy; francesco.orsini@polito.it (F.O.); domenico.ferrero@polito.it (D.F.); massimo.santarelli@polito.it (M.S.)

² Energy Center, Politecnico di Torino, Via P. Borsellino 38/16, 10138 Turin, Italy

* Correspondence: davide.papurello@polito.it

Abstract: Apparent kinetics is often used to describe a variety of reactions in the field of chemical looping and solar thermochemical processes, yet a rigorous analytical methodology for utilizing such kinetics has been lacking. The implementation of a novel approach was exemplified in the ceria thermochemical cycle for producing solar thermochemical hydrogen, specifically in the H₂O-driven oxidation step. The H₂ production rate equation was derived, rearranging apparent kinetics from experimental data in the literature into a more suitable analytical form. The 1D model integrates heat transfer, fluid dynamics, and redox chemistry, providing the description of a directly irradiated solar receiver–reactor. Model robustness is ensured through the oxygen mass balance across the cycle, and the comparison against experimental data shows high agreement. The methodology can be useful for simulating chemical looping cycles using any nonstoichiometric oxide, such as ceria-based oxides and, most importantly, oxidation-limited perovskites, for which optimizing the oxidation step in terms of fluid flow, kinetics, and reaction times is crucial. The proposed analytical model can be applied to arbitrarily complex reactor geometries. The inherently local nature of the model also allows the spatial distributions of the redox material’s conversion and utilization to be obtained, paving the way for optimization strategies of the reactor’s design and operation.

Keywords: solar thermochemical hydrogen; solar reactor; numerical modelling; apparent kinetics; nonstoichiometric oxygen carrier



check for updates

Academic Editor: Ioan Sarbu

Received: 17 December 2024

Revised: 14 January 2025

Accepted: 16 January 2025

Published: 18 January 2025

Citation: Orsini, F.; Ferrero, D.; Papurello, D.; Santarelli, M. Solar Thermochemical Fuel Production: A Novel, Validated Multiphysics Reactor Model for the Reduction–Oxidation of Nonstoichiometric Redox Cycles. *Energies* **2025**, *18*, 414. <https://doi.org/10.3390/en18020414>

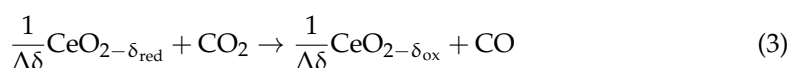
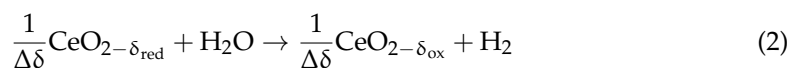
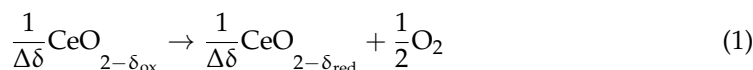
Copyright: © 2025 by the authors. Licensee MDPI, Basel, Switzerland. This article is an open access article distributed under the terms and conditions of the Creative Commons Attribution (CC BY) license (<https://creativecommons.org/licenses/by/4.0/>).

1. Introduction

Solar-driven thermochemical cycles can be considered valuable systems for clean energy production, contributing to the green energy transition [1,2]. In a recent review, Tran et al. [3] reported how the thermochemical option to produce solar green hydrogen (or equivalently, solar syngas) is more promising than other routes, such as photovoltaic-driven or biomass-based alternatives, that suffer, respectively, from a restricted usable wavelength range for solar energy conversion, and several logistical challenges. From this perspective, thermochemical cycles aimed at synthetic fuel generation via H₂O and/or CO₂ splitting are currently being intensively investigated [4–9]. Splitting reactions are facilitated by making use of reactive solid intermediates while being energetically optimized based on respective thermodynamic constraints [10]. Solid intermediates used for oxygen transfer reactions are referred to as oxygen carriers (OCs), typically metal oxides or perovskites [11,12]. Currently, there is strong interest within the scientific community in nonstoichiometric OCs, such as

ceria and perovskites, because these materials can maintain their lattice structure without undergoing phase changes upon redox cycling, resulting in improved stability [3,13].

Nonstoichiometric ceria ($\text{CeO}_{2-\delta}$) is considered the state-of-the-art OC for thermochemical splitting due to its fast oxidation kinetics and good cyclic durability [7]. In nonstoichiometric thermochemical splitting, the $\text{H}_2\text{O}/\text{CO}_2$ splitting reaction is decomposed into two cyclic reaction steps that equal the overall splitting reaction when summed up. In the cycle, the OC is first thermally reduced at high temperature (up to 1673–1873 K [14]) and low O_2 partial pressure, thereby releasing O_2 from the lattice up to the equilibrium of the reaction (Equation (1)). In the following oxidation step (Equations (2) and (3)), the OC is oxidized back when subjected to a high $\text{H}_2\text{O}/\text{CO}_2$ partial pressure, resulting in H_2/CO production at a typically lower oxidation temperature (below 1273 K). Nonstoichiometry variation $\Delta\delta := \delta_{\text{red}} - \delta_{\text{ox}}$ ($[\text{mol}_\text{O} \cdot \text{mol}_\text{OC}^{-1}]$), referred to as oxygen exchange capacity [15] or oxygen storage capacity [16], gives a measure of the exchanged O_2 across the redox cycle and correlates to the fuel produced in the oxidation step. Intensive research effort is being directed towards solar-assisted thermochemical splitting [3,17], in which concentrated solar thermal energy is used to thermally feed the process due to the high theoretical solar-to-fuel efficiencies coming from the full utilization of the solar spectrum, as well as from the direct solar radiation conversion into process heat [3,18].



Numerous concepts of solar reactors for efficiently running solar-driven thermochemical splitting are proposed in the literature, mostly with ceria-based OCs. Consequently, several attempts to rationally classify such numerous systems are proposed. According to Lu et al. [13], the classification can be made by differentiating in the following: (i) systems that involve the movement of the redox material in space (either self-supporting structures—including monoliths, Reticulated Porous Ceramics (RPCs), and 3D-printed hierarchically channelled structures [3]—or particles), with the gas streams and operating temperatures kept constant in each different reaction chamber; and (ii) systems in which the redox material is fixed in space (either self-supporting structures or fixed beds of particles), with the gas streams and operating temperatures adjusted cyclically in time according to the reaction step that is ongoing. The same differentiation criteria are mentioned by Weber et al. [19]. The recent review by Tran et al. [3] alternatively classifies solar thermochemical reactors in the following two broad categories: self-supporting reactors and particle-based reactors. Whereas monolithic and RPC-based reactors would fall into the former category, all moving/non-moving particle-containing reactors would fall into the latter. The reader is redirected to the cited comprehensive reviews [3,13] for further details on the classification and description of solar thermochemical devices, which are beyond the scope of this work. Recent novel concepts include both particle-based systems and self-supporting monolithic/RPC-based systems. In the former category, Weber et al. [19] proposed a process referred to as SOMPIHR (Swept, Open Moving Particle Reactor Including Heat Recovery), consisting of a particle receiver followed by a moving bed heat exchanger performing the particles' thermal reduction while subjected to inert (N_2) sweeping, and subsequently a counter-current oxidation reactor chamber. In the latter category, a new monolithic receiver–reactor concept was reported by Brendelberger et al. [20], referred to as a receiver–reactor cavity system with multiple mobile redox units (R2Mx). The R2Mx

concept involves moving reactive material in the form of monoliths instead of particles between different reaction zones, allowing for their continuous operation and solid–solid heat recovery. Modelling results were reported recently [21]. Following a similar philosophy, a new multi-reactor concept in the form of a reactor train system was proposed at the Massachusetts Institute of Technology [22], consisting of a series of indirectly irradiated, ceria RPC moving reactors operating dynamically and capable of implementing solid–solid heat recovery in a counterflow radiative heat exchanger configuration. It should also be mentioned for completeness that attempts to perform thermochemical splitting reactions in a fluidized bed configuration were considered [23,24].

Regardless of the working principle and design of the specific reactor concept, the full development of solar thermochemical technology would require—among other features—an easy scale-up of the system [3]. In [13], the authors highlight the technical difficulties in scaling up receiver–reactors with moving redox-active parts due to the need to manage and have thorough control of the moving parts together with the reduction/oxidation atmospheres to which they are subjected while the system is at a high temperature and with the necessity of avoiding gas leakages between the different chambers. Similar concerns were also raised by Tran et al. [3], who reported how the moving parts in solar thermochemical reactors should be minimized because of the likely failures upon high-temperature operation, generating reliability challenges. On the other hand, Lidor and Bulfin [17] recently reported a critical analysis of the two-step thermochemical fuel production technology, defining the key performance indicators that should be considered when evaluating its further development, namely reactor efficiency, power output, power density, and oxidant feedstock conversion. Specifically, the power density of volumetric directly irradiated receiver–reactors tested by Zoller et al. [25] was reported to be sufficiently low, raising questions about the practical feasibility of further scaling up this specific reactor concept [17]. Nonetheless, this directly irradiated, volumetric reactor design allowed the highest solar-to-fuel efficiencies to be reached to date at around 5.25% and 5.6% for 4 kW and 50 kW scales, respectively [3,25,26].

It is, thus, clear how the preliminary design of such systems is of the utmost importance to predict the reactor behaviour and performance, and specifically, detailed heat and mass transfer modelling at the receiver–reactor level is required to guide the engineering process.

An excellent review on solar thermochemical reaction systems modelling was recently reported by Wheeler et al. [27]. Many modelling works have appeared in the literature in recent years, trying to capture the complex multiphysics featured by such systems and at different levels of detail. A representative overview of modelling works from the literature is summarized in Table 1, with details on the reactor typology and governing equations implemented for mass and momentum conservation, as well as for heat transfer and chemistry. Most of the works reported so far have focused on the reduction step of the cycle [28–38], mainly assuming a thermodynamic equilibrium (e.g., in [31,38]), with few pioneering works addressing the detailed surface solid–gas interface kinetics [28,29] and rarely applying apparent kinetic laws [34,39]. Li et al. [35] modelled an isothermal flow reactor featuring the downward flow of ceria particles undergoing thermal reduction in contrast to an upward gas flow. The authors explored the effects of reaction kinetics as well as the design and operational parameters (i.e., reactor length and particle diameter) on the reduction extent observed. For reduction kinetics, results were reported using both the models developed by Keene et al. [28,29] and Bulfin et al. [40], interestingly showing how the rate parameters can be calibrated to take into account the transition from the kinetics-limited regime to the thermodynamics and gas advection-limited regime when dealing with different reactor designs and material morphologies. Zhang and Smith [36] proposed a 3D transient model of a directly irradiated, inert-swept partition-cavity solar

thermochemical reactor with a packed bed of CeO_2 particles as the reactive material. The authors investigated the fluid flow and heat transfer behaviour as a function of several geometric factors, such as the partition gap size, the catalyst thickness, and the inlet/outlet position, giving insight into optimal configurations based on the resulting flow and temperature fields. The reduction kinetics for each CeO_2 particle was modelled following Ishida et al. [41]. Some other works were focused on the thermal and/or thermomechanical behaviour of the reactor [42–44] without implementing reaction kinetics. Interestingly, relatively limited efforts in simulating the oxidation step were found, in which either the oxidation is supposed to be sufficiently fast to impose thermodynamic equilibrium [45] or trends are assumed for nonstoichiometry upon oxidation in the absence of kinetic rate expressions for this latter cycle step [46]. Venstrom et al. [47] developed an equilibrium model for both the reduction and oxidation steps of the ceria redox cycle, considering a fixed bed reactor. However, while the model predicts the release rate of O_2 upon reduction in a wide temperature range of 740–1500 °C, it is not applicable for estimating the production rates of CO during oxidation at temperatures below 930 °C, as the oxidation becomes limited by surface kinetics. The same authors [48] then developed a three-dimensional, transient model of a solar reactor for splitting CO_2 in the isothermal ceria cycle at a high temperature (1500 °C), at which global reaction rates are driven by advective mass transport rates and intrinsic material thermodynamics. The model implemented the rate of expression developed by Bulfin et al. [40], which was properly modified by imposing the thermodynamic equilibrium constraint coupled with the direct thermal CO_2 dissociation to determine the resulting CO produced at high temperatures. Pan et al. [49] proposed a steady-state model for heat and mass transfer coupled to chemical kinetics in an oxygen-permeable membrane reactor. The model developed by Bulfin et al. [40] was implemented to describe the reduction kinetics. On the oxidation side, the apparent kinetic law presented by Le Gal et al. [50] was rearranged and used, taking into account the dependence of the rate on temperature and solid conversion. However, this kinetic law did not take into account the dependence of the reaction rate on the partial pressure of CO_2 in the reacting gas stream, which can have an impact on the resulting kinetics, as widely stated elsewhere [39,51]. Wang et al. [52] recently proposed a dual-scale one-dimensional model for the ceria redox cycle. This model integrates the transport of species in the porous bed (macroscopic scale) and the transport of lattice oxygen within the particles (mesoscopic scale) and implements the detailed surface and bulk kinetics developed by Zhao et al. [53] for the ceria system. The redox cycle consists of an H_2 -assisted reduction and an H_2O dissociation step. The authors found that the oxidation process is faster than the reduction but that the transport at the macroscopic and mesoscopic scales is of the same order of magnitude. In recent work, Dai et al. [54] modelled the ceria water-splitting cycle, taking into account the kinetics of both thermal reduction and H_2O -driven oxidation, with a similar approach proposed by Bala Chandran et al. [48] and expressing the rate parameter as a function of temperature and the reacting surface area. No further works were found implementing a complete splitting kinetics, neither for CO_2 nor for H_2O dissociation, considering a thermal-driven reduction step. It is also worth stressing that although studying the oxidation step imposing chemical equilibrium results in enlightening considerations concerning the highest efficiency achievable by a thermochemical cycle, this only represents the ideal boundaries of the process operation. As a matter of fact, reaction kinetics also has a significant role in determining the overall productivity and feasibility, as reported very recently by de la Calle et al. [55], thereby suggesting that the reactor design should take these considerations into account.

Table 1. Selected works on thermochemical splitting reactor modelling from the literature compared with the present work.

Reference	Dimensions, Numerical Method, and Software	OC and Reactor	Mass and Momentum Conservation	Energy Conservation	Radiative Heat Transfer	Chemistry and Kinetics
Lapp et al. [42], 2013	2D model.	No OC reactions implemented. Counter-rotating cylinders reactor with solid–solid heat recovery.	n.a.	LTE is assumed between the solid and gas phases.	RDA and Monte Carlo ray tracing.	No kinetics implemented (only thermal model).
Lapp et al. [46], 2014	Transient 3D model.	Isotropic porous ceria ($\epsilon = 0.75$). Counter-rotating cylinders reactor with solid–solid heat recovery.	n.a.	LTE is assumed between the solid and gas phases.	RDA. The surface is assumed to be opaque.	Equilibrium is implemented. Reduction is supposed to be “fast”; oxidation is supposed to reach near-completion at the temperatures predicted in the oxidation zone. Nonstoichiometry is supposed to decrease linearly to zero across the oxidation zone in the absence of kinetic rate expressions.
Keene et al. [28], 2013	Axisymmetric cylindrical domain. Finite volume method with in-house-developed Fortran code.	Porous ceria ($\epsilon = 0.75$) supposed homogeneous, isotropic, dimensionally stable. Directly irradiated.	Mass conservation is formulated for solid and gas phases and for individual components of the fluid phase (i.e., argon and oxygen). Darcy’s law is used for momentum conservation.	LTNE—each phase (solid and gas) is described with its own energy equation.	Radiatively participating solid; radiatively nonparticipating gas. RDA for the optically thick medium is implemented. The irradiated boundary is treated as a black surface.	Solid–gas interface kinetics is implemented. A model is developed for the adsorption/desorption of oxygen across the solid–gas interface to accurately describe the kinetics in terms of the local T , p_{O_2} , and δ . Only reduction is simulated.
Keene et al. [29], 2014	1D model. Finite volume method with in-house-developed Fortran code.	Porous ceria monolith. Cavity-type, directly irradiated.	Mass conservation is formulated for solid and gas phases and for individual components of the fluid phase (i.e., argon and oxygen). Darcy’s law is used for momentum conservation.	LTNE—each phase (solid and gas) is described with its own energy equation.	Radiatively participating solid; radiatively nonparticipating gas. The internal radiative heat transport is modelled with RDA.	Solid–gas interface kinetics is implemented. Kinetics is implemented through the model developed by Keene et al. [28]. A constant kinetic rate is enforced for it to be sufficiently high and simulate equilibrium chemistry (i.e., transport-limited regime). Only reduction is simulated.
Bala Chandran et al. [30], 2015	3D model of a single reactive element. Transport equations are solved in ANSYS Fluent 14.0.1.	Porous ceria supposed homogeneous, isotropic, with constant porosity ($\epsilon = 0.65$) and a specific surface area. Cylindrical cavity, directly irradiated.	Mass conservation is formulated for solid and gas phases, considering interfacial mass transfer due to oxygen release upon reduction. Momentum transport is formulated using the Darcy–Brinkman–Forchheimer model.	LTE is assumed between the solid and gas phases.	Radiatively participating solid; radiatively nonparticipating gas. Internal radiative heat transport modelled with RDA.	Solid–gas interface kinetics is implemented. Kinetics is implemented through the model developed by Keene et al. [28]. Only reduction is simulated.

Table 1. Cont.

Reference	Dimensions, Numerical Method, and Software	OC and Reactor	Mass and Momentum Conservation	Energy Conservation	Radiative Heat Transfer	Chemistry and Kinetics
Bala Chandran et al. [48], 2016	Transient 3D model developed in ANSYS Fluent 15.0.	Isothermal, pressure-swing ceria redox cycle. Packed bed ($\epsilon_{\text{bed}} = 0.45$) of ceria porous particles ($\epsilon_p = 0.75$).	Volume-averaged mass and momentum conservation. Brinkman–Forchheimer law is used for momentum conservation. Binary mass diffusivities obtained from the Chapman–Enskog theory.	LTE is assumed between the solid and gas phases.	Combination of Monte Carlo ray tracing and a discrete ordinates model.	Reduction and CO ₂ -driven oxidation are simulated. The kinetics from Bulfin et al. [40] is used, imposing the thermodynamic equilibrium constraint coupled with the CO ₂ thermal dissociation at high temperatures.
Bader et al. [43], 2015	3D finite element model.	Isothermal, pressure-swing ceria redox cycle. Porous ceria particles, with mm scale porosity. Packed-bed cavity, indirectly irradiated (alumina tubes for the single reactive elements). Pressure drop and effective thermal conductivity are compared for a 65% porous monolith, packed bed of 5 mm, 70% porous particles, 5 μm solid particles, and 92% porous RPC.	Extended Darcy’s law is used for the pressure drop estimation.	LTE is assumed between the solid and gas phases.	Monte Carlo ray tracing and RDA.	Thermal and linear elastic thermo-mechanical model of the isothermal redox cycle. No kinetics implemented.
Wang et al. [56], 2021	3D heat and mass transfer model.	Iron–manganese oxides. Packed-bed reactor.	Mass and species conservation equations are solved separately for each phase. The momentum equation is solved only for the gas phase (the solid phase is immobile).	LTNE—each phase (solid and gas) is described with its own energy equation.	Radiative transport equation.	Global kinetics is implemented.
Lidor et al. [31], 2020	1D model. MONROE code (developed at DLR).	Macroporous ceria. ASTOR reactor.	Darcy–Dupuit–Forchheimer law is used.	LTNE—each phase (solid and gas) is described with its own energy equation.	RDA combined with Beer–Lambert law.	Equilibrium is implemented for ceria reduction (deduced/supposed).
Lidor et al. [45], 2021	1D model. MONROE code (developed at DLR).	Macroporous ceria. ASTOR reactor.	Darcy–Dupuit–Forchheimer law is used. Oxygen exchange upon cooldown sweeping seems to be neglected.	LTNE—each phase (solid and gas) is described with its own energy equation.	RDA combined with Beer–Lambert law.	Equilibrium is implemented for ceria reduction (as in Lidor et al. [31]) and oxidation (this latter is “supposed to be fast at every point in the reactor at each time step”).

Table 1. Cont.

Reference	Dimensions, Numerical Method, and Software	OC and Reactor	Mass and Momentum Conservation	Energy Conservation	Radiative Heat Transfer	Chemistry and Kinetics
Furler et al. [32], 2015	In-house code, ANSYS CFX 14.0.	Single-scale porosity RPC ceria. Cavity receiver–reactor.	Mass, momentum, and species conservation equations expressed for the free-flow domains and for the porous RPC domain. Momentum source according to Dupuit–Forchheimer law.	An interphaseal heat transfer coefficient is used, but LTE is imposed in practice by setting it artificially high (since diffusion is dominant over advection).	Radiative transfer equation. Radiatively participating RPC.	Only reduction is simulated, assuming equilibrium. “The reduction was modelled based on thermodynamic equilibrium, as previous work has shown that the overall kinetics were controlled by heat transfer”.
Zoller et al. [33], 2019	2D axisymmetric model. ANSYS CFX 17.0.	Dual-scale porosity RPC ceria. Cavity receiver–reactor.	n.a.	An interphaseal heat transfer coefficient is used, but LTE is imposed in practice by setting it artificially high.	Radiative transfer equation. Radiatively participating RPC.	Only reduction is simulated, assuming equilibrium. Heat transfer model.
Wang et al. [52], 2022	1D model. Axial macroscopic combined with radial mesoscopic model.	Porous ceria with a fixed bed. Directly irradiated.	Permeability tensor and flow resistance coefficient modelled by the Ergun equation.	LTNE. A radial mesoscopic heat transfer equation is also added to the solid phase.	P-1 model.	Reaction kinetics from Zhao et al. [53] is implemented for the H ₂ -driven reduction and for the H ₂ O dissociation.
Dai et al. [54], 2022	1D model developed in COMSOL Multiphysics® 5.3.	Macroporous ceria. Directly irradiated.	Darcy–Brinkman–Forchheimer model is used for momentum conservation.	LTNE.	P-1 model.	The kinetics of both thermal reduction and H ₂ O-driven oxidation are simulated with a similar approach, as proposed by Bala Chandran et al. [48] and expressing the rate parameter as a function of temperature and the reacting surface area.
Pan et al. [49], 2021	2D axisymmetric steady-state model. COMSOL Multiphysics® (software version not specified).	Oxygen-permeable ceria membrane reactor.	Navier–Stokes equations in the gas phase, and no porous media (ceria dense membrane). Binary mass diffusion coefficients obtained from the Fuller–Schettler–Gilding equation. Oxygen ion migration in the membrane described by Fick’s law.	No porous media. Convective heat transfer in the gas phase and conductive heat transfer in the membrane. Simplified isothermal wall assumption.	Radiation is not modelled.	Reduction kinetics according to Bulfin et al. [40]. Oxidation kinetics according to Le Gal et al. [50]. A constant rate of modification was included to take into account the surface reaction on the ceria membrane.

Table 1. Cont.

Reference	Dimensions, Numerical Method, and Software	OC and Reactor	Mass and Momentum Conservation	Energy Conservation	Radiative Heat Transfer	Chemistry and Kinetics
Li et al. [35], 2020	3D model. ANSYS Fluent 17.1.	Single-tube reactor featuring a downward ceria particle flow in contrast to an upward inert gas flow for ceria reduction.	Discrete particle phase studied with a Lagrangian-tracking approach. Gas phase resolved as a continuum with an Eulerian volume-averaged approach. Ambipolar diffusion is modelled within the ceria particles.	Isothermal conditions: $T_{\text{red}} = T_{\text{gas}} = T_{\text{particle}}$.	Radiation is not modelled.	Reduction kinetics is modelled according to Keene et al. [28,29] and Bulfin et al. [40].
Zhang and Smith [36], 2019	3D transient model. Soltrace software and STAR-CCM+ 12.02.	Directly irradiated, inert-swept partition-cavity solar thermochemical reactor, with a packed bed of CeO ₂ particles as the reactive material.	Mass conservation in the fluid and particle phases are coupled, defining a CeO ₂ particle mass transfer rate from the rate equation as the O ₂ source.	The energy transfer between the fluid phase and the discrete particles is modelled through a convective heat transfer coefficient between the two phases.	Radiative transfer equation in the packed bed of particles.	Reduction kinetics is modelled according to Ishida et al. [41].
Huang and Lin [44], 2021	3D steady-state non-isothermal model. COMSOL Multiphysics® (software version not specified).	Windowed (directly irradiated) and window-less (indirectly irradiated) designs.	Brinkman equations are implemented for mass and momentum conservation.	LTNE.	P1 approximation in the porous medium coupled with surface-to-surface radiation within the cavity and window.	Chemistry is not modelled.
Ma et al. [37], 2024	3D transient model.	Directly irradiated receiver–reactor containing a porous structure made of CeO ₂ -ZrO ₂ . Details on the morphology are not given explicitly.	Brinkman equations are implemented for mass and momentum conservation.	Heat transfer assumption in the porous medium not explicitly reported.	Approximation used not clearly stated.	Reduction kinetics is modelled according to Bulfin et al. [40].
Wei et al. [57], 2024	ANSYS Fluent 16.0 coupled with the Monte Carlo method.	Dense ceria tubular membrane reactor integrated with heat recovery for continuous fuel production.	The Darcy–Brinkman–Forchheimer model is used for momentum conservation.	LTNE in the alumina RPC.	Radiative transfer equation.	Kinetics is not implemented.
Lougou et al. [58], 2018	Model developed in COMSOL Multiphysics® 5.3.	Porous NiFe ₂ O ₄ .	Brinkman equations are implemented for mass and momentum conservation in the porous medium.	Heat transfer assumption in the porous medium not explicitly reported.	RDA in the porous medium coupled with surface-to-surface radiation.	Chemistry is not modelled.

Table 1. Cont.

Reference	Dimensions, Numerical Method, and Software	OC and Reactor	Mass and Momentum Conservation	Energy Conservation	Radiative Heat Transfer	Chemistry and Kinetics
Li et al. [38], 2016	3D transient heat transient model.	Indirectly irradiated cavity receiver–reactor; array of tubular absorbers with ceria particles and packed bed loading.	Fluid flow governing equations are not reported (only heat transfer and thermal reduction model).	LTE.	Collision-based Monte Carlo ray tracing model inside the cavity. RDA in the porous bed.	Only reduction is simulated. Ceria is supposed to be at thermodynamic equilibrium (i.e., no kinetics is modelled), according to Bulfin et al. [40].
This work	1D model developed in COMSOL Multiphysics® 6.2.	Macroporous ceria. Directly irradiated.	Darcy–Forchheimer law is used. Binary mass diffusivities obtained from the Chapman–Enskog theory.	LTNE.	RDA.	Reduction kinetics is modelled according to Bulfin et al. [40]. Oxidation kinetics is modelled according to Arifin et al. [59], rearranging the apparent kinetic law into a local kinetic law.

In the present work, a multiphysical model of a ceria-based, inert-swept, directly irradiated structured receiver–reactor was developed for a simplified geometry, implementing the reaction kinetics for both thermal reduction and H₂O-driven oxidation steps and simulating the entire cycle, making use of apparent kinetics extracted from experimental data in the literature. The model implementation was validated through accurate comparison with experimental data for both reduction and oxidation steps, revealing excellent agreement. A simple approach is proposed to implement apparent kinetics in solar thermochemical nonstoichiometric reaction systems—such as ceria-based or perovskite materials—when the reactants’ partial pressure plays an active role in determining the material kinetics. The analytical model presented, specifically applied here to the H₂O-driven oxidation step, allows the conversion of the global kinetic law into a local kinetic law, which can be coupled to other physics in reactor-level models, filling a gap in the current literature. The proposed novel analytical methodology is thought to be useful when modelling any solid–gas reaction for which apparent kinetics can be retrieved from experiments [39] and, as a local approach, can be extended to arbitrarily complex solar reactor geometries. The inherently local nature of the model also allows for optimization strategies of the reactor’s design and operation at the same time in terms of spatial distributions of the OC’s reactivity and efficient utilization.

For a more extensive discussion of the model applications, the reader is redirected to Section 4. The model implementation is presented in detail in Section 2, with the novel analytical methodology specifically described in Section 2.4.2 and the validation of the experiments shown in Section 2.10. Section 3 shows the key results from the model, while the conclusions of the work are summarized in Section 5.

2. Model

The model, run in a commercial finite element analysis software (COMSOL Multiphysics[®], release 6.2), solves the complete ceria redox cycle, composed of thermal reduction under an inert swept gas flow (N₂) and H₂O-driven oxidation for hydrogen production. The inert-swept reduction option was investigated in the literature as one of the possible oxygen removal strategies, with predictions of viable efficiencies when suitable heat recovery strategies are implemented [60]. Also, previous modelling works assumed the occurrence of inert sweep during reduction, both for the volumetric receiver–reactor [31] and counter-current, direct-contact particle-based reactor [19] concepts. Reaction kinetics is solved together with heat and mass transport across the porous OC. A 1D geometry is considered, with the domain corresponding to the porous structure irradiated from one end. Figure 1 visualizes the 1D geometry represented as a cylinder, although no radial coordinates were considered in the model. The OC’s diameter and irradiated area (Table 2) are used in the model to define the pointwise mass flux in fluid flow physics and to define the cross-sectional area of the domain in heat transfer physics. Similar models were developed in the literature [31,45,52,54], but either thermodynamic equilibrium was assumed for both steps of the cycle [45] instead of detailed redox kinetics, H₂-assisted reduction was considered [52], or different approaches for the kinetics treatment were followed, such as by applying the law of mass action and introducing an oxidation rate parameter to be related to the kinetics of the reaction [54]. Below 1000 °C, H₂O-driven ceria oxidation is reported to be controlled by surface kinetics rather than thermodynamics [54,61], calling for the modelling investigation of the oxidation kinetics when dealing with temperature swing redox cycles. Thus, to the best of our knowledge, there is a lack of heat and mass transport models that readily and easily implement the redox kinetics of the entire thermally driven cycle, utilizing apparent kinetic laws derived from experimental data. Despite the research effort to model the ceria thermochemical cycle with this apparent solid-state kinetics approach [51,59], only sparse examples can be found in the literature making use of this form of the rate equation

at the reactor level, and without clear details on their implementation. This kind of kinetic law can be extracted from any material intended to be modelled for this application, and the rate equation takes the same analytical form. This gives our approach a wide applicability, as highlighted in Section 4. The governing physics implemented in the model are reported below.

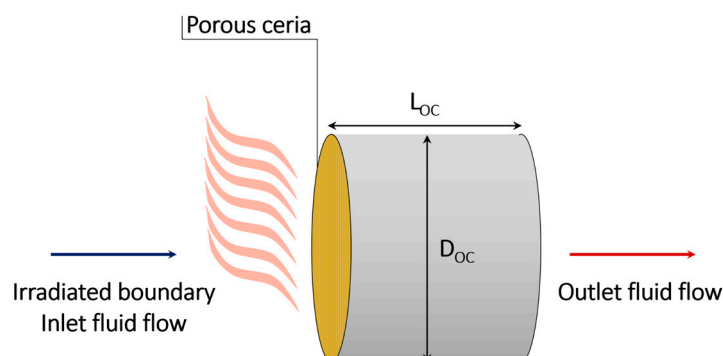


Figure 1. The 1D geometry simulated in this work represented as a cylinder for better visualization (i.e., no radial coordinates were considered in the model).

2.1. Geometry

The geometric parameters adopted in the model are reported in Table 2.

Table 2. Geometric parameters adopted in the model.

Geometric Parameter	Value	Units
OC thickness, L_{OC} [31]	0.060	m
OC diameter, D_{OC} [62]	0.046	m

2.2. Mass and Species Conservation

The species balance takes into account the N_2/O_2 mixture upon thermal reduction (i.e., O_2 released by ceria) and the $N_2/H_2O/H_2$ mixture upon H_2O -driven oxidation. Nitrogen has been used as an inert gas in both the reduction and oxidation steps of the model to adjust the partial pressure of reactants to the levels of the references adopted for the kinetics. A background O_2 molar fraction of 10^{-6} was maintained during the oxidation as well. The latter choice was made to ensure the validity of the kinetic law selected during the reduction step [40], obtained in the oxygen partial pressure range of 10^{-2} – 10^{-8} bar. This is also coherent with real systems in which achieving ideal gas tightness from external ambient air is not practically feasible. Notice that previous works implemented the H_2O splitting equilibrium and used the equilibrium O_2 partial pressure as the parameter driving the thermodynamics without including O_2 in the mass balance and in the chemical species transport [63]. Although this could be readily performed in the model presented herein, this would imply using the equilibrium nonstoichiometry function outside of the validity range. Thus, as a first choice, a fixed O_2 partial pressure was imposed. This aspect will be detailed in follow-up models, considering the full oxygen partial pressure dependence and suitable equilibrium nonstoichiometry functions and/or experimental data. A concentrated species model was also employed, in which the chemical species were assumed to be present in the mixture in comparable amounts rather than having a predominant component with the other being present in minor amounts, and the mixture's properties were then evaluated as a function of the mixture's composition. The equation that solves for the mass fraction ω_i of the i th species in the fluid phase is the following:

$$\rho_f \frac{\partial \omega_i}{\partial t} + \nabla \cdot \mathbf{j}_i + \rho_f (\mathbf{u} \cdot \nabla) \omega_i = R_i \quad (4)$$

$$\mathbf{j}_i = - \left(\rho_f D_i^f \nabla \omega_i + \rho_f \omega_i D_i^f \frac{\nabla M_n}{M_n} - \rho_f \omega_i \sum_k \frac{M_i}{M_n} D_k^f \nabla x_k \right) \quad (5)$$

$$M_n := \left(\sum_i \frac{\omega_i}{M_i} \right)^{-1} \quad (6)$$

Here, R_i is the rate of the species source or sink coming from the solid–gas reactions, as detailed in Section 2.4; x_k is the molar fraction of the k th species in the ideal gas mixture; M_i is the molar mass of the i th species; and D_i^f is the diffusion coefficient of the i th gas in the mixture, following Equations (7)–(9) according to the Chapman–Enskog theory [64].

$$D_i^f = \left(\sum_{\substack{j=1 \\ j \neq i}}^n \frac{x_j}{D_{ij}} \right)^{-1} \quad (7)$$

$$D_{ij} = \frac{0.00266 T^{\frac{3}{2}}}{p M_{ij}^2 \sigma_{ij}^2 \Omega_D} \quad (8)$$

$$M_{ij} := 2 \left[\left(\frac{1}{M_i} \right) + \left(\frac{1}{M_j} \right) \right]^{-1} \quad (9)$$

Here, σ_{ij} is the characteristic length, and Ω_D represents the diffusion collision integral, the function of the gas species, and temperature [64].

2.3. Momentum Conservation

Since the problem deals with low flow rates and, thus, low Reynolds numbers (<100), the flow regime is assumed to be laminar. The flow analysis is performed using the Darcy–Forchheimer law:

$$\nabla p = - \frac{\mu_f}{K} \mathbf{u} - F \rho_f |\mathbf{u}| \mathbf{u} \quad (10)$$

The fluid viscosity is denoted by μ_f , the permeability is denoted by K , the Forchheimer coefficient is denoted by F , and the fluid density is denoted by ρ_f . Details on the effective transport properties can be found in Section 2.8, whereas the physical properties of the fluid and solid phases are summarized in Section 2.7.

2.4. Reaction Kinetics

2.4.1. Thermal Reduction

During thermal reduction, the redox kinetics proposed by Bulfin et al. [40] are implemented via Equation (11), with δ being the nonstoichiometry, as defined in Equations (1)–(3). $\delta_{\max} = 0.35$ resulted in the maximum value that δ could reach in order to retain the ceria fluorite phase and keep the kinetic equation valid [40].

$$\frac{d\delta}{dt} = (\delta_{\max} - \delta) A_{\text{red}} e^{-\frac{E_{\text{red}}}{R_g T}} - \delta P_{\text{O}_2}^{n_{\text{O}_2}} A_{\text{ox}, \text{O}_2} e^{-\frac{E_{\text{ox}, \text{O}_2}}{R_g T}} \quad (11)$$

Then, the oxygen source R_{O_2} , expressed as $\left[\frac{\text{kg}_{O_2}}{\text{m}^3\text{s}}\right]$, for the oxygen transport equation was derived as follows, with ε being the ceria porosity:

$$R_{O_2} = \frac{(1 - \varepsilon)\rho_{CeO_2}M_{O_2}}{2M_{CeO_2}} \frac{\partial\delta}{\partial t} := \Lambda^{\text{red}} \frac{\partial\delta}{\partial t} \quad (12)$$

The proportionality constant between the nonstoichiometry variation and the mass source was defined as Λ^{red} for simplicity. In the model, the reverse partial differential equation (PDE), Equation (13), was then solved to find the nonstoichiometry field, $\delta(x, t)$, across the porous medium.

$$\frac{\partial\delta}{\partial t} = \frac{R_{O_2}}{\Lambda^{\text{red}}} \quad (13)$$

Kinetic parameters are summarized in Table 3.

Table 3. Kinetic parameters adopted in the model [40,59].

Kinetic Parameter	Value	Units
A_{red}	720,000	s^{-1}
E_{red}	232	kJ mol^{-1}
A_{ox,O_2}	82	$\text{s}^{-1} \text{bar}^{-n_{O_2}}$
E_{ox,O_2}	36	kJ mol^{-1}
n_{O_2}	0.218	1
A_{ox,H_2O}	1	s^{-1}
E_{ox,H_2O}	29	kJ mol^{-1}
γ	0.89	1

2.4.2. H₂O-Driven Oxidation

For the oxidation step, apparent kinetics from the solid-state reaction theory [39] is adapted, starting from the kinetic law experimentally found by Arifin et al. [59], as given in Equation (14):

$$\frac{d\alpha}{dt} = k(T)f(\alpha)h(x_{H_2O}) \quad (14)$$

$$k(T) = A_{\text{ox},H_2O} e^{\frac{-E_{\text{ox},H_2O}}{R_g T}} \quad (15)$$

$$f(\alpha) = 1 - \alpha \quad (16)$$

$$h(x_{H_2O}) = x_{H_2O}^\gamma \quad (17)$$

The solid conversion α , spanning from 0 (start of the reaction) to 1 (reaction completed), expresses the reaction progress. The temperature dependence is separately embedded in the rate constant, expressed through Equation (15) when written in the Arrhenius formulation, with A_{ox,H_2O} being the preexponential factor and E_{ox,H_2O} being the apparent activation energy for the oxidation reaction. Equation (16) models the dependence on the reaction progress. The dependence from the i th gas reactant concentration—here expressed in terms of the molar fraction, x_i —is included through the $h(x_i)$ function. The power law functional form shown in Equation (17), in which γ is the reaction order [51], assumes that gaseous products are efficiently removed from the reaction zone such that the backward reduction reaction is prevented [39]. Kinetic parameters are collected in Table 3. This kinetic analysis reported by Arifin et al., in agreement with thermodynamic data published by Panlener et al. [65], ensures that the ceria oxidation can proceed up to completion (zero nonstoichiometry) in the operating conditions investigated, apart from kinetic limitations. According to this kinetic law, the H₂O-driven ceria oxidation can be expressed through a first-order model (F1). In the reference work [59], the apparent kinetic

parameters were extracted after having stripped all the experimental artifacts coming from the setup—such as gas-phase dispersion, oxidant mixing, and detector time lag—from the mass spectrometry signals in order to correctly obtain the intrinsic kinetic behaviour of the process. We should also mention that, in order to be reliable, this type of rate equation requires thorough control of the experimental conditions from which they are obtained; in particular, the experimental procedure should ensure that the set-point temperature, that is, the temperature value used in the kinetic fitting, equals the sample's temperature [39]. This also means that heat and mass transfer limitations during the experimental kinetic tests should be minimized via accurate verification against the sample mass [66]. These precautions lead to uniform reactivity throughout and, thus, to an accurate correlation between the experimental conditions imposed (temperature, gas atmosphere) and observed reaction rate.

The used kinetic law describes the water-splitting reaction over ceria, making use of a single-step rate equation [39]; that is, the reaction can be fully described using one single kinetic mechanistic model [59]. However, as a further necessary consideration, it is worth mentioning that even if the apparent kinetic law can be expressed using one single mechanism, this does not necessarily mean that the reaction under investigation proceeds in one single step [39]. It is rather the case that the slowest step in the reaction mechanism controls the overall reaction rate, resulting in the observed apparent kinetics [39]. In this specific case, the water-splitting reaction over nonstoichiometric ceria was reported to feature a multi-step mechanism involving surface and bulk diffusion steps, as described by Zhao et al. [53]. Thus, using this kind of rate equation involves inherent reliability in simulating the overall reaction dynamics; nonetheless, a relatively low computational complexity can be pursued since the detailed single reaction steps do not need to be implemented one by one.

Apparent kinetic laws of this type are usually obtained experimentally as global bulk correlations. However, the global kinetic information needs to be converted into local terms in order to be implemented in reactor modelling. We can, thus, assume that the apparent kinetic law was obtained in sufficiently controlled experimental conditions where the sample reacted uniformly without heat or mass transfer limitations and that the extracted kinetic parameters are representative of a point-like, uniform reaction. For this aim, the solid conversion α is here expressed as follows:

$$\alpha(x, t) := \frac{\delta_0(x) - \delta(x, t)}{\delta_0(x) - \delta_\infty(x, t)} \quad (18)$$

This allows the solid conversion α to be expressed as a function of the nonstoichiometry δ of the OC instead of as a function of the sample mass, thereby addressing a local dependence instead of a global bulk dependence. $\delta_0(x) := \delta(x, t = 0)$ is the nonstoichiometry field at the initial time (i.e., just after the reduction step), while $\delta_\infty(x, t)$ is the nonstoichiometry towards which the ceria system converges in the thermodynamic equilibrium limit, and it is expressed according to Bulfin et al. [40] as a function of the local temperature and oxygen partial pressure:

$$\delta_\infty(T, p_{O_2}) = \delta_{\max} \frac{8700 p_{O_2}^{n_{O_2}} e^{-\frac{195.6[\text{kJmol}^{-1}]}{R_g T}}}{1 + 8700 p_{O_2}^{n_{O_2}} e^{-\frac{195.6[\text{kJmol}^{-1}]}{R_g T}}} \quad (19)$$

$\delta_{\max} = 0.35$ has the same meaning as in Equation (11). Equation (18) can be rearranged as follows:

$$\delta_0(x) - \delta(x, t) = \alpha(x, t) \cdot [\delta_0(x) - \delta_\infty(x, t)] \quad (20)$$

Thus, differentiating both sides of the equation and taking into account the stoichiometry of the oxidation reaction (Equation (2)), the H_2 mass source term expressed in $\left[\frac{\text{kg}_{H_2}}{\text{m}^3\text{s}}\right]$ is derived and implemented in the following respective transport equation

$$R_{H_2} = \frac{(1 - \varepsilon)\rho_{CeO_2}M_{H_2}}{M_{CeO_2}} \left\{ [\delta_0(x) - \delta_\infty(x, t)]A_{ox, H_2O} e^{-\frac{E_{ox, H_2O}}{R_g T(x, t)}} (1 - \alpha(x, t))x_{H_2O}^\gamma(x, t) - \frac{\partial \delta_\infty(x, t)}{\partial t} \alpha(x, t) \right\} \quad (21)$$

Notice that a term depending on the thermodynamic equilibrium state of the system appears explicitly (i.e., the last term on the right-hand side: $-\frac{\partial \delta_\infty(x, t)}{\partial t} \alpha(x, t)$), with a boosting effect on the oxidation kinetics when the equilibrium nonstoichiometry δ_∞ rapidly decreases due to the switching operating conditions passing from the reduction to the oxidation step (i.e., this term becomes positive when $\frac{\partial \delta_\infty(x, t)}{\partial t}$ is negative). Moreover, notice that we simplified the dependence notation for the equilibrium nonstoichiometry since $\delta_\infty(T, p_{O_2}) = \delta_\infty(T(x, t), p_{O_2}(x, t)) = \delta_\infty(x, t)$. The H_2O mass sink (expressed as a negative source) follows directly:

$$R_{H_2O} = -\frac{M_{H_2O}}{M_{H_2}} R_{H_2} \quad (22)$$

Thus, the final form of the PDE solved by the model during the oxidation phase is as follows:

$$\frac{\partial \delta}{\partial t} = \frac{R_{H_2}}{\Lambda^{ox}} \quad (23)$$

with the definition where $\Lambda^{ox} := -\frac{(1 - \varepsilon)\rho_{CeO_2}M_{H_2}}{M_{CeO_2}}$. Notice that the oxidation kinetics depend only on the reactant (H_2O) concentration, and not on the chemically reducing product of the oxidation reaction, which is consistent with the kinetic law.

For the sake of completeness, we should also mention that in the case that the mass transfer or diffusion limits the reaction at the reactor level, the rate equation could require some calibration in order to adequately fit the up-scaled system with respect to the reference lab-scale setup, similarly to Li et al. [35]. Although this point is not directly addressed in the present work because of the simple 1D configuration, the authors are considering these aspects of detail in advanced 2D+ model simulations that include more complex OC morphologies, and results will be reported in upcoming publications. To further accentuate this point, we stress that the oxidation model validation (see Section 2.10) was performed using exactly the same kinetic parameters used in the reference work [59], leading to excellent agreement with our model results.

2.5. Energy Conservation

For energy conservation, the Local Thermal Non-Equilibrium (LTNE) assumption between the solid and fluid phases is adopted. Thus, a single energy equation for each phase is implemented. The solid phase is considered as radiatively participating, while the gas phase is modelled as radiatively nonparticipating, as commonly assumed throughout the literature (see Table 1).

The energy conservation for the solid phase is given by Equation (24), with the equivalent radiative flux expressed in the conductive form (see Section 2.8) following Equation (25), the reaction heat following Equations (26) and (27), and the oxygen vacancy formation enthalpy for ceria obeying Equation (28), with this latter following the work of

Bulfin et al. [67]. The specific surface area A_{sf} and the interfacial heat transfer coefficient h_{sf} are calculated from correlations in the literature (see Section 2.8).

$$(1 - \varepsilon)\rho_{CeO_2} \frac{\partial}{\partial t} (c_{p,CeO_2} T_s) = (1 - \varepsilon)\nabla \cdot (k_s \nabla T_s) + A_{sf} h_{sf} (T_f - T_s) + \dot{q}_r + \dot{q}_c \quad (24)$$

$$\dot{q}_r = \nabla \cdot (k_r \nabla T_s) \quad (25)$$

$$\dot{q}_{c,red} = \frac{-2\Delta h_{red}(\delta)}{M_{O_2}(1 - \varepsilon)} R_{O_2} \quad (26)$$

$$\dot{q}_{c,ox} = \frac{\Delta h_{red}(\delta) - \Delta h_{H_2O,diss}}{M_{H_2}(1 - \varepsilon)} R_{H_2} \quad (27)$$

$$\Delta h_{red}(\delta) = 10^3 \cdot \left(478 - 1158\delta + 1790\delta^2 + 23368\delta^3 - 64929\delta^4 \right) \left[\frac{J}{mol} \right] \quad (28)$$

Notice that the exothermic heat from the oxidation phase was neglected in previous works [45]. Moreover, it can be noticed that the global oxidation kinetics being used in this work was obtained in the temperature range of 750–950 °C [59]. Exothermic heat increases the temperature in the domain, leading to operations in a temperature range slightly out of the validity range of the kinetic law. However, this approximation is considered valid for this work, and this kinetic law was implemented here in the absence of alternative correlations.

The fluid phase consists of a mixture of N_2/O_2 during reduction and of $N_2/H_2/H_2O$ during oxidation, with all the thermophysical properties summarized in Section 2.7. The corresponding energy conservation is given by the following equation:

$$\varepsilon \frac{\partial}{\partial t} (\rho_f c_{p,f} T_f) + \varepsilon \rho_f c_{p,f} \mathbf{u} \cdot \nabla T_f = \varepsilon \nabla \cdot (k_f \nabla T_f) + A_{sf} h_{sf} (T_s - T_f) \quad (29)$$

Thus, the reaction heat is assumed to develop in the solid phase and to be transferred to the fluid phase by interfacial convection.

2.6. Initial and Boundary Conditions

2.6.1. Initial Conditions

The initial conditions adopted in the model are reported in Table 4. In the simulations, the first cycle starts from a steady system at ambient temperature. Ceria is supposed to be fully oxidized (i.e., $\delta(t = 0) = 0$) at the beginning of the first redox cycle, which starts with the reduction step. All the following cycles use the previous solution as new initial values for all the relevant solution fields (i.e., nonstoichiometry, nonstoichiometry time derivative, absolute pressure, and solid and fluid temperature). This is valid for both reduction and oxidation steps. At the beginning of the oxidation step, the H_2O concentration is supposed to switch linearly from zero up to the nominal x_{H_2O} considering an imposed switching time of 1 min. This is consistent with real systems, in which an ideally instantaneous switching front cannot be established and facilitates the transition from reduction to oxidation by reducing computational instabilities.

Table 4. Initial and boundary conditions adopted in the model.

Initial or Boundary Condition	Value	Units
Mass and species conservation		
Initial O_2 molar fraction (first reduction)	10^{-6} (balance N_2)	1
Initial H_2 molar fraction (oxidation)	0	1
Initial H_2O molar fraction (oxidation)	0	1
Inlet O_2 molar fraction (reduction and oxidation)	10^{-6} (balance N_2)	1
Inlet H_2 molar fraction (oxidation)	0	1
Inlet H_2O molar fraction (oxidation) (base case parametric range)	0.2 0.2–0.4 (balance N_2)	1

Table 4. Cont.

Initial or Boundary Condition	Value	Units
Momentum conservation		
Initial pressure (first reduction)	1	bar
Inlet volume flow rate during reduction (base case parametric range)	1 0.5–2	L/min
Inlet volume flow rate during oxidation	1	L/min
Outlet pressure	1	bar
Reaction kinetics		
Initial nonstoichiometry (first reduction)	0	1
Initial nonstoichiometry time derivative (first reduction)	0	1/s
Heat transfer		
Initial temperature (first reduction)	25	°C
Inlet fluid temperature (reduction oxidation)	25 300	°C
Incident radiative power (reduction oxidation)	1.5 0.5	kW
Inlet boundary	Re-radiation towards $T_{amb} = 298.15K$	-
Outlet boundary	Thermal insulation	-
Other		
Oxidation switching time	60	s
Step duration (reduction oxidation) (first cycle)	5000 600	s

2.6.2. Boundary Conditions

Together with the initial conditions, the boundary conditions implemented in the model are reported in Table 4. The inlet volume flow rate was chosen in the order of 1 L/min to be coherent with the gas analysis equipment of our laboratory [68], which will be used in future prototype experimental campaigns to validate the model. Also, the radiative power was chosen coherently with our solar dish receiver [69] (with a nominal concentrated power of 2.8 kW in optimal conditions and temperatures up to 1800 °C), which will be used in future experimental testing. The cycle steps' duration matches the values assumed in the work of Lidor et al. [31] and Arifin et al. [59] for reduction and oxidation, respectively.

2.7. Physical Properties

Thermophysical properties for the solid phase (ceria) and of the gas mixture are summarized in Table 5, with the properties of single gasses taken from the NIST database [70].

Table 5. Thermophysical properties assumed in the model.

Property	Value	Units
Ceria		
Porosity	0.7	1
Molar mass	172.115 [31]	kg/kmol
Density	7215 [31]	kg/m ³
Thermal conductivity	0.5615 [31]	W m ⁻¹ K ⁻¹
Heat capacity at constant pressure	$67.95 - \frac{9.9 \cdot 10^5}{T^2} + 0.0125 \cdot T$ [71] M_{CeO_2}	J kg ⁻¹ K ⁻¹
Gas mixture		
Density	Molar fraction averaged	kg/m ³
Thermal conductivity	Molar fraction averaged	W m ⁻¹ K ⁻¹
Specific heat capacity	Mass fraction averaged	J kg ⁻¹ K ⁻¹
Viscosity	Molar fraction averaged	Pa s

2.8. Morphological and Effective Transport Properties

The porous ceria structure is considered a statistically homogeneous and isotropic macroporous medium, corresponding with the morphology correlations used in [72]. It should be noted that alternative and more efficient structures were engineered recently for thermochemical fuel processing, such as RPC monoliths featuring dual-scale porosity [26]

or even hierarchically channelled structures [73]. Thus, the analysis conducted in this work is detailed and can be extended to more sophisticated and efficient porous structures in follow-up studies. It is noted how some previous works also considered dual-scale porosity RPC structures with a surface absorption–emission model coupled with a lumped capacity model, thus neglecting the volumetric radiative heat transfer needed to reduce the computational cost [22]. Herein, the porosity ε was fixed at 0.7, a value already used in previous modelling works for similar morphologies [31,45]. The specific surface area A_{sf} and the mean pore diameter d_m were considered to be a function of ε following Equations (30) and (31), according to Suter et al. [72].

$$A_{sf} = -2277.8\varepsilon^2 + 2533\varepsilon + 262.3 \quad (30)$$

$$d_m = 2.2 \cdot 10^{-3} \varepsilon + 7.59 \cdot 10^{-4} \quad (31)$$

Both the permeability K and Dupuit–Forchheimer coefficient F appearing in the momentum conservation equation are described by Equations (32) and (33), following the corrected Carman–Kozeny model and Cooke’s correlation, respectively [72].

$$K = \frac{\varepsilon^{3.5}}{4.81 A_{sf}^2} \quad (32)$$

$$F = \frac{9.81 \cdot 10^{-6}}{K^{1.12}} \quad (33)$$

The Nusselt number (Nu) for computing the interfacial heat transfer coefficient, $h_{sf} := \frac{k_f Nu}{d_m}$, which models the LTNE is described by Equation (34) [72], with $Re := \rho u_D d_m / \mu$ and $Pr := \mu c_p / k_f$ [74].

$$Nu = 5.54 + \left(0.709\varepsilon^2 - 0.631\varepsilon + 0.298\right) Re^{\sqrt{1.7-1.39\varepsilon}} Pr^{0.6} \quad (34)$$

The internal radiative heat transfer is modelled with the Rosseland Diffusion Approximation (RDA) for optically thick media [75], which is widely used in the literature for simulating solar reactor systems [28–31,43,45,46]. Thus, the effective radiation conductivity k_r is computed as per Equation (35), in which β_R is the Rosseland mean extinction coefficient following Equation (36) [72,76], σ is the Stefan–Boltzmann constant, and n is the refractive index of the medium, assumed to be unity in this study [29,30]. Although RDA represents the simplest way to model the internal radiative heat transfer in this type of system [27], it is assumed to be valid for this work, which focuses on the implementation of the redox kinetics using a simple analytical approach that can fit a large number of solar thermochemical nonstoichiometric reaction systems and can also be coupled to more complex radiation modelling methodologies. More detailed radiation modelling will be addressed in follow-up works.

$$k_r = \frac{16n^2 \sigma T_s^3}{3\beta_R} \quad (35)$$

$$\beta_R = \frac{1.765\sqrt{1-\varepsilon}}{d_m} \quad (36)$$

2.9. Numerical Methods and Computational Optimization

The mesh of the 1D domain was refined until the grid independence was achieved. Both a uniform mesh and an increasing-size cell mesh were compared, with the latter appearing to be more suitable for capturing the fast radiative heating at the boundary during reduction. Thus, the cell size was finer at the irradiated inlet boundary and became

coarser towards the outlet boundary. The grid independence was checked, taking the O₂ production rate at 2000 s during the reduction step of the first cycle when the time derivative was large. Spanning from 50 to 10⁴ cells, a final value of 1500 increasing-size cells was selected (with a maximum-to-minimum cell size ratio of 3), as this value ensures that grid independence is achieved while balancing computational cost. An in-software adaptive time-stepping scheme was adopted, with the initial time step maintained at a sufficiently low level (<10⁻⁶ s) in all the simulations, to better catch the fast initial dynamics of the process in both cycle steps—fast radiative heating upon reduction and fast H₂ generation upon oxidation. This model solves the time dependency using the second-order Backward Difference Formula (BDF) and a direct, fully coupled solver.

2.10. Validation

The model was validated through comparison with experimental data from the literature for both reduction and oxidation steps, extending the simulation to a more accurate 2D axisymmetric geometry. The reduction model was compared against data from Davenport et al. [61], with the reference experimental conditions summarized in Table 6. As shown in Figure 2a,b, the comparison at 50 °C/min and 150 °C/min heating ramps was reported, respectively, and the O₂ production rate and the cumulative O₂ yield from the model simulation matched the experimental profiles with high agreement. Slight differences were attributed to experimental uncertainty, such as the rate of measurement and the instantaneous temperature of the sample, as well as the inlet gas.

Table 6. Experimental conditions implemented in the simulation for reduction model validation [61].

Parameter	Experimental Value [61]
Ceria mass (g)	0.46
Ceria bulk porosity (-)	0.86
Inner diameter (cm)	0.635
Temperature ramp (°C/min)	50 or 150
Initial temperature (°C)	805
Final temperature (°C)	1488
Inlet flow rate (sccm)	463
O ₂ inflow (ppm)	10.8
Reference conditions	0 °C, 1 atm

The oxidation model results in terms of the hydrogen production rate profile were validated against data from Arifin et al. [59], with the referenced experimental conditions summarized in Table 7. As depicted in Figure 3, the H₂ production rate curve in time agrees well with the experimental profile. As clearly stated in the reference work [59], the delay in the onset of the H₂ signal was due to the dispersion, mixing, and detector time lag inherent to the experimental apparatus and not to the water-splitting chemistry. After an initial lag of around 100 s, the simulated profile followed the experimental rate profile with excellent agreement.

Table 7. Experimental conditions implemented in the simulation for oxidation model validation [59].

Parameter	Experimental Value [59]
Ceria mass (g)	0.15
Wall/inlet temperature (°C)	800
Reactor pressure (torr)	75
Inlet flow rate (sccm)	500
H ₂ O inflow molar fraction (-)	0.2
Reduction temperature (°C)	1500
Reduction pressure (torr)	600

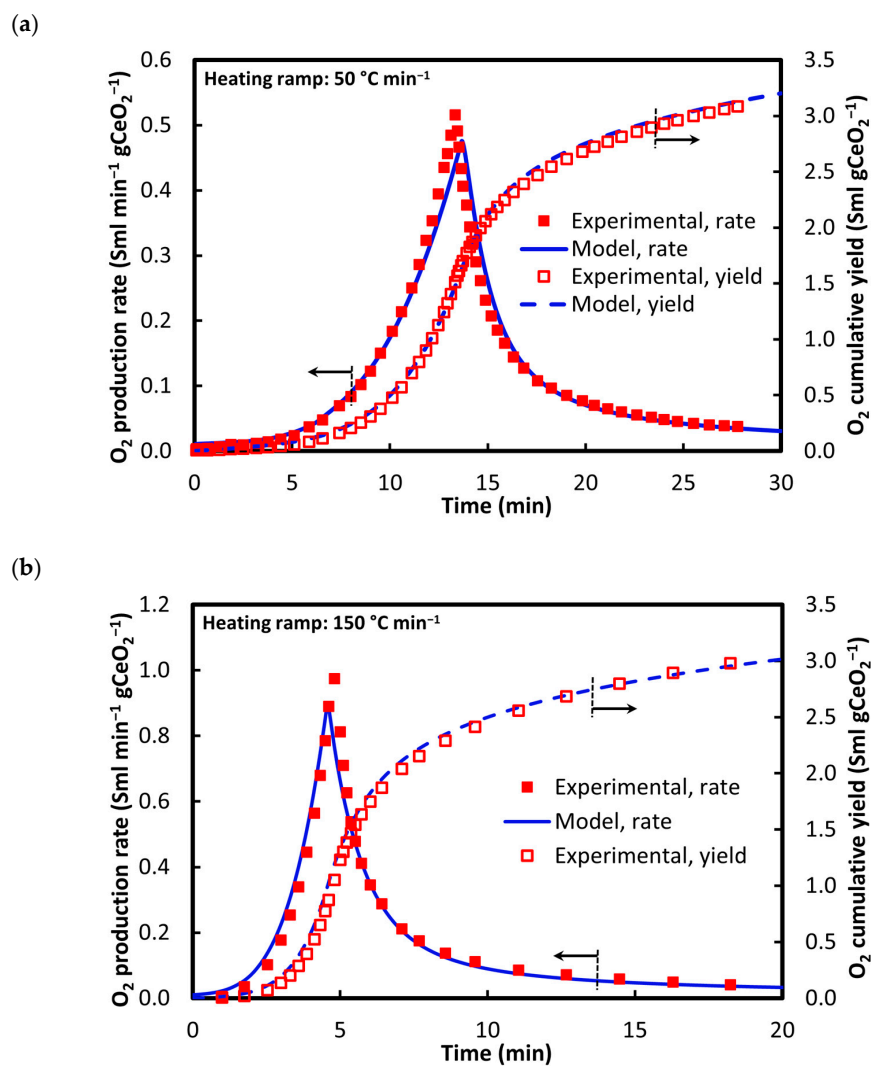


Figure 2. Validation of the reduction model. Experimental data are taken from [61], with heating ramps of (a) $50\text{ }^{\circ}\text{C min}^{-1}$ and (b) $150\text{ }^{\circ}\text{C min}^{-1}$. Black arrows indicate the y-axis the curves refer to (O_2 production rate: left axis; O_2 cumulative yield: right axis).

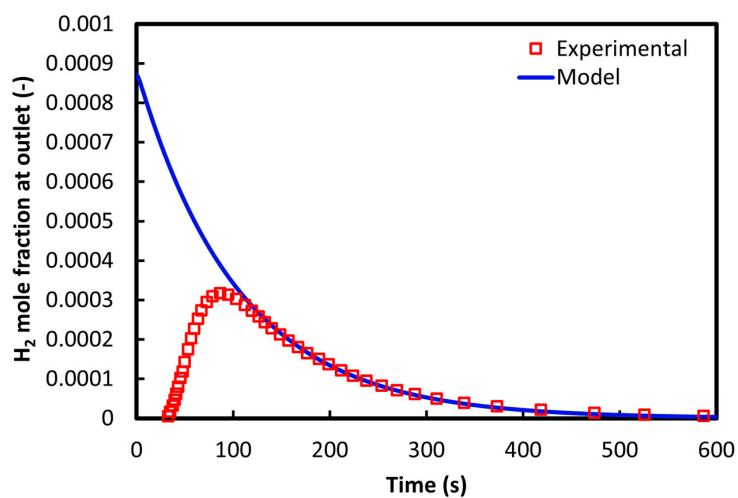


Figure 3. Validation of the oxidation model. Experimental data are taken from [59].

3. Results and Discussion

First, results on the first redox cycle are reported to demonstrate the robustness of the model. Concerning reduction (Section 3.1), the results are reported in terms of the temperature and oxygen partial pressure fields in the porous medium, as well as in terms of the nonstoichiometry distribution achieved. Concerning oxidation (Section 3.2), results are reported, most notably in terms of nonstoichiometry and solid conversion distribution in the porous medium. As mentioned, this capability of the model discloses the possibility to extend the spatial distribution analysis even in complex geometries and to synergically optimize the redox material's utilization and reactivity with fluid flow and heat transfer. Then, the results in terms of the nonstoichiometry field and hydrogen production rates are observed upon tuning some design and operational parameters, such as the inert mass flow rate and the H₂O concentration in the feed (Sections 3.3.1 and 3.3.2). It must be highlighted that parametric studies on similar systems are already available in the literature, with a close look at the effect of inert gas inlet temperature and mass flow, radiation flux on the exposed boundary, and porosity [31], as well as porosity distributions [54]. However, this detailed and extensive parametric investigation fully makes sense when dealing with more specific reactor geometries, for which operational parameters are already well-defined [45]. This calls for the model's extension to higher dimensionality beyond 1D simulations, and ongoing investigations made by the authors are addressing these upgrades. Thus, although the model is not geometry-specific (apart from considering consistent geometrical features from the literature—see Table 2), qualitative information on the system's operation is extracted from the kinetic simulations and from narrowed parametrization to assist future studies involving higher dimensionality. Most importantly, besides experimental validation, the validity of the redox model is further demonstrated by looking at the oxygen balance in the redox cycle. As such, optimal conditions can be implemented in a multiple-cycling simulation to directly observe the stabilization of the numerical solutions.

3.1. Reduction: 1st Cycle (Base Case)

Figure 4 shows the system's behaviour during the first reduction step, considering the initial heating of the system at a constant incident radiative power of 1.5 kW and lasting 5000 s. This amount of time is more than sufficient to reach typical ceria reduction temperatures of around 1500 °C, with steady-state heating compensated by re-radiation losses at the inlet boundary in the present simulation. Temperature and oxygen partial pressures in the system, which govern the redox thermodynamics, are reported in Figure 4a,b against the spatial coordinate. The results are coherent with previous modelling works in terms of similar temperature, oxygen partial pressure, and nonstoichiometry trends [28,31], corroborating the validity of the physics implementation. Figure 4a reports the solid and fluid temperature in space, showing that interfacial convection is large enough to ensure thermal equilibrium between the two phases from just a few millimetres behind the irradiated boundary. A temperature gradient develops, with steady-state temperatures at the outlet section at around 1450 °C. The oxygen partial pressure in the porous medium tends first to increase in the first half of the porous bed (curve after 1000 s, Figure 4b) and to stabilize to an equilibrium value, with oxygen being advected downstream [28]. With temperature gradually increasing at deeper lengths in the porous medium, the oxygen starts to be released accordingly until the reactivity starts to decrease because the equilibrium state is being approached. Figure 4c-d show the nonstoichiometry field across the porous medium against the spatial coordinate and, in time, with a nonstoichiometry gradient developing along the porous structure as a consequence of its optical thickness and leading to a larger extent of reduction near the irradiated boundary under the assumptions of this work. As a result, the thermodynamic equilibrium is practically achieved along the whole length

(Figure 4d) since the δ and δ_∞ curves appear to be overlapped along the entire reduction duration. Local equilibrium was already experimentally observed for ceria-based compositions during thermal reduction in previous reports [40,77], in which the reduction reaction was limited by heat transfer (i.e., experimental heating ramps). The molecular oxygen released upon the first reduction amounted to around 6.5 mmol in the reactive bed, against 62.7 mmol, which could be obtained with a uniform nonstoichiometry of 0.1 in the entire domain.

It is worth mentioning that a highly non-uniform nonstoichiometry distribution across the porous active material, such as the one observed in our simplified 1D geometry (Figure 4c), represents a bad utilization of the redox active material, and as such, a source of inefficiency in the process. In this specific case, the low nonstoichiometry in the downstream part of the 1D reactor mainly came from the increasing p_{O_2} along the flow direction, which hindered further reduction in the investigated conditions. Alternatively, the same undesired behaviour can be observed if the volumetric radiative absorption is not sufficiently effective to ensure a uniform temperature distribution—remember that we are implementing simplified assumptions for the internal radiative heat transfer here. Overall, the design of efficient solar receiver–reactors should pursue reduction across the active material that is as uniform in its extent as possible [73] in order to efficiently utilize the available OC and maximize the fuel production yield. Thus, it appears clear how detailed multiphysics modelling, such as the geometrically simplified case proposed herein, is of paramount importance for an efficient reactor design, allowing the prediction of possible sources of inefficiencies needing optimization and refinement.

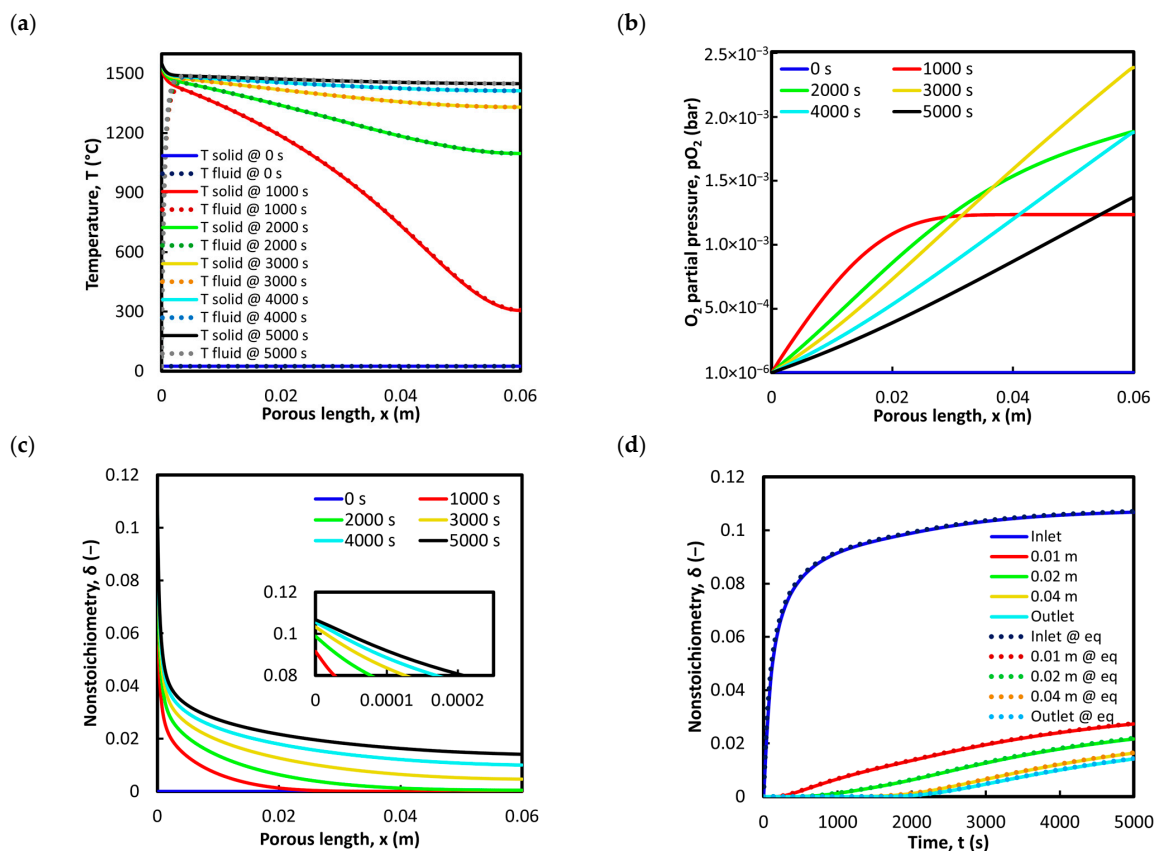


Figure 4. Results from the reduction step of the first redox cycle. (a) Temperature, (b) oxygen partial pressure, and (c) nonstoichiometry in space at different time instants. (d) Nonstoichiometry in time at different locations in the porous domain. Solid lines: actual nonstoichiometry. Dotted lines: equilibrium nonstoichiometry.

3.2. Oxidation: 1st Cycle (Base Case)

After the first reduction, the solution fields at 5000 s were taken as the initial conditions for running the oxidation step. The water inflow was not setup as a step-function plug flow, but a switching time of 1 min was imposed to reach the nominal water concentration linearly in time. As mentioned, this is consistent with real systems, in which a perfect plug flow front cannot be realized and reduces computational instabilities during transition. Figure 5a,b depict the nonstoichiometry field evolution in the porous domain, in space and in time, respectively. The left part of the domain oxidizes faster due to the higher water content of the entering flow. As shown, 10 min is sufficient time to oxidize the entire domain, with nonstoichiometry almost uniformly approaching zero after 5 min. Similar information can be gathered from Figure 5c,d, showing the evolution of the solid conversion field in a specular way, and approaching the unity value after 300 s. Figure 5e shows the H_2 source in the ceria domain at different time instants, with fast reactivity in the exposed boundary, and a production peak shifting in the flow direction as the reaction progresses to completion. Figure 5f reports the hydrogen volumetric flow rate at the outlet along the entire oxidation step. A sharp peak appears at the beginning, with the maximum located just after the water has reached the nominal inflow concentration at the imposed switching time of 60 s, and then decreasing to near-zero values in less than 500 s. The total hydrogen produced in the first oxidation step gives reoxidation to the extent of unity in terms of the oxygen mass balance, confirming the consistency of the redox model. Also, a radiative input of 0.5 kW was imposed to thermally sustain the reaction. However, in principle, this feature could be modulated and controlled dynamically or even turned off during the oxidation phase of the cycle. Here, this external power was maintained to ensure a steady-state temperature in the range of 900–1000 °C upon oxidation, and it is the operating range of our concentrating solar dish [69] that will be used in future experimental campaigns. The solid-phase temperature evolution is depicted in Figure 5g, also shows the steady-state profile after 600 s. Notice how the temperature at the outlet keeps a flat slope because of the thermal insulation boundary hypothesis. Notice also how the exothermic heat is not released or lost towards the external part along the porous domain under the 1D assumption of this work.

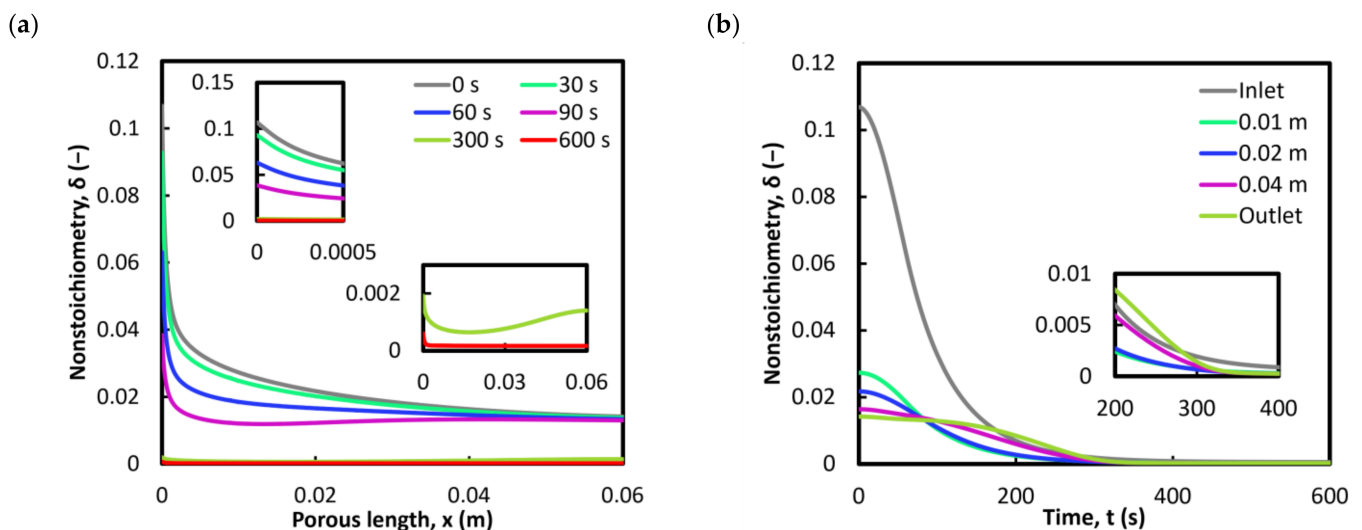


Figure 5. Cont.

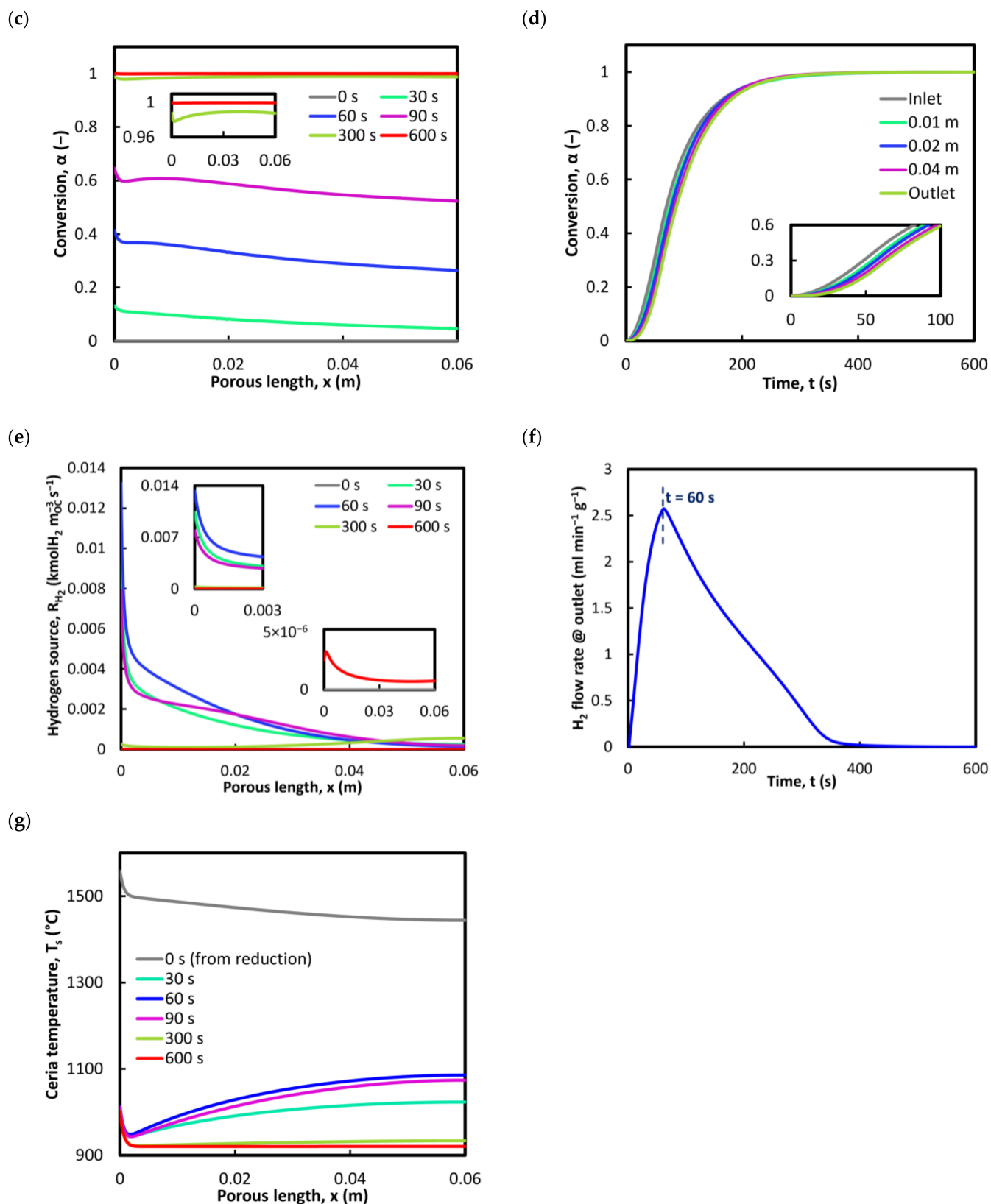


Figure 5. Results from the oxidation step of the first redox cycle. (a) Nonstoichiometry, (c) solid conversion, (e) hydrogen source, and (g) solid-phase temperature in space at different time instants. (b) Nonstoichiometry and (d) solid conversion in time at different locations in the porous domain. (f) Outlet hydrogen volumetric flow rate in time.

3.3. Parametric Study

The thermochemical performance of volumetric, directly irradiated solar receiver–reactors is highly dependent on the morphological features of the reactive porous absorber [72]. The porosity and specific surface are considered the most relevant factors impacting the effective transport properties of the porous medium. Bulk porosity was previously investigated as one of the parameters that can be tuned to control the reactor behaviour. Lidor et al. [31] reported how an increase in this feature leads to a lower average temperature throughout the porous bed, and thus to a lower nonstoichiometry, and eventually to a lower overall reduction extent. A promising direction is to consider non-uniform porosities across the active bed, allowing the radiation to penetrate deeper into the porous structure, thereby allowing a more uniform temperature field [73]. A higher porosity at the irradiated boundary would allow for deeper penetration of the incoming radiation, which is an effect that was addressed in similar previous studies through the Beer–Lambert exponential law coupled with RDA [31,45]. Interestingly, Dai et al. [54] investigated continuous porosity distribution functions in the porous medium. The authors revealed that a higher porosity on both boundaries could be beneficial for the system’s performance since this configuration reduces the radiation losses from the front boundary and the conduction losses from the solid phase from both boundaries, insulating the reactor core. However, in the absence of radiative attenuation effects as supposed in the present work, a change in the porosity would have a direct effect, only on the equivalent radiative thermal conductivity through the porosity-dependent extinction coefficient. Thus, this effect is not addressed here and will be described in future works where the redox kinetics will be coupled to a more detailed radiative heat transfer model. Moreover, when dealing with porosity, the overall ceria load in the reactor, i.e., the effective density of the structure, defined as the ceria mass per total volume, is considered one of the most important performance metrics in this kind of solar reactor since a trade-off between a sufficiently high effective density and sufficient uniform heating in the structure should be addressed [73]. A parametric study addressing the porosity in such a way as to not impact this indicator would, thus, be reasonable in principle.

Maintaining the porosity as uniform in space and fixed for all the simulations, the parameters studied herein, impacting the redox kinetics, are the inert flow rate during the reduction step and the water concentration during the oxidation step.

3.3.1. Sweeping Gas Flow Rate During Reduction

Figure 6 shows the impact on the system behaviour of a variation in the sweeping N_2 flow rate during the first reduction, considering both a halved value and a doubled value compared to the base case (1 L/min). Figure 6a,b report the ceria temperature and the O_2 partial pressure in the system against the spatial coordinate, respectively, which govern the reduction thermodynamics and directly impact the nonstoichiometry. After 1000 s, an increased sweeping flow rate (2 L/min) led to higher temperatures in the solid phase, reaching 640 °C at the outlet against 180 °C achieved at the halved flow rate (0.5 L/min) and around 300 °C with 1 L/min. The highest flow rate also leads to the lowest temperature gradients along the solid domain, which is beneficial for the system. This trend is explained by looking at the interfacial heat transfer contribution. For a higher flow rate, the interfacial solid-to-fluid heat transfer at the entrance is higher, and the fluid reaches higher temperatures near the inlet. Also, the fluid reaches the colder region of the domain faster, where the fluid-to-solid heat transfer also increases for higher sweeping flow rates. This induces higher and more uniform temperatures in the solid phase, as observed. The opposite applies at lower flow rates. After 5000 s, the solid temperature profiles appear closer, with the highest flow rate profile appearing more uniform, with lower temperature

values in the first half of the domain. This effect is also shown in Figure 6c, depicting the ceria temperature in time. Because of the interfacial heat transfer, the ceria temperature at the outlet (and in the whole domain) increases much more rapidly, with 1000 °C achieved at the outlet in 40% less time at 2 L/min than at 0.5 L/min (Figure 6c). Thus, in the range of flow rates investigated, a higher sweeping gas flow rate induced faster heating and more uniform temperature profiles in the reactive solid phase, which is beneficial for the process's performance and thermal stability. The flow rate impact on the partial pressure of O₂ in the system is shown in Figure 6b. As expected, the higher the sweeping gas flow rate, the lower the pO₂. After 1000 s, the plateau effect showed a delay at higher flow rates. The higher temperature and lower O₂ partial pressure distributions coming from a higher sweeping flow rate induce a response in terms of the higher reduction extent, as depicted in Figure 6d. The nonstoichiometry at the outlet (least exposed) section reaches a 0.01 value two-thirds of the time with 2 L/min against 0.5 L/min. It should be noted that at higher and higher sweeping gas flow rates beyond the range investigated herein, a reversed effect was expected to arise, as pointed out by Lidor et al. [31]. Indeed, a very high sweeping gas flow rate entering at a relatively low temperature would generate faster cooling near the inlet and an overall lower temperature along the entire domain. However, an extensive and comprehensive parametric analysis goes beyond the scope of this work, which is more focused on the implementation of redox physics.

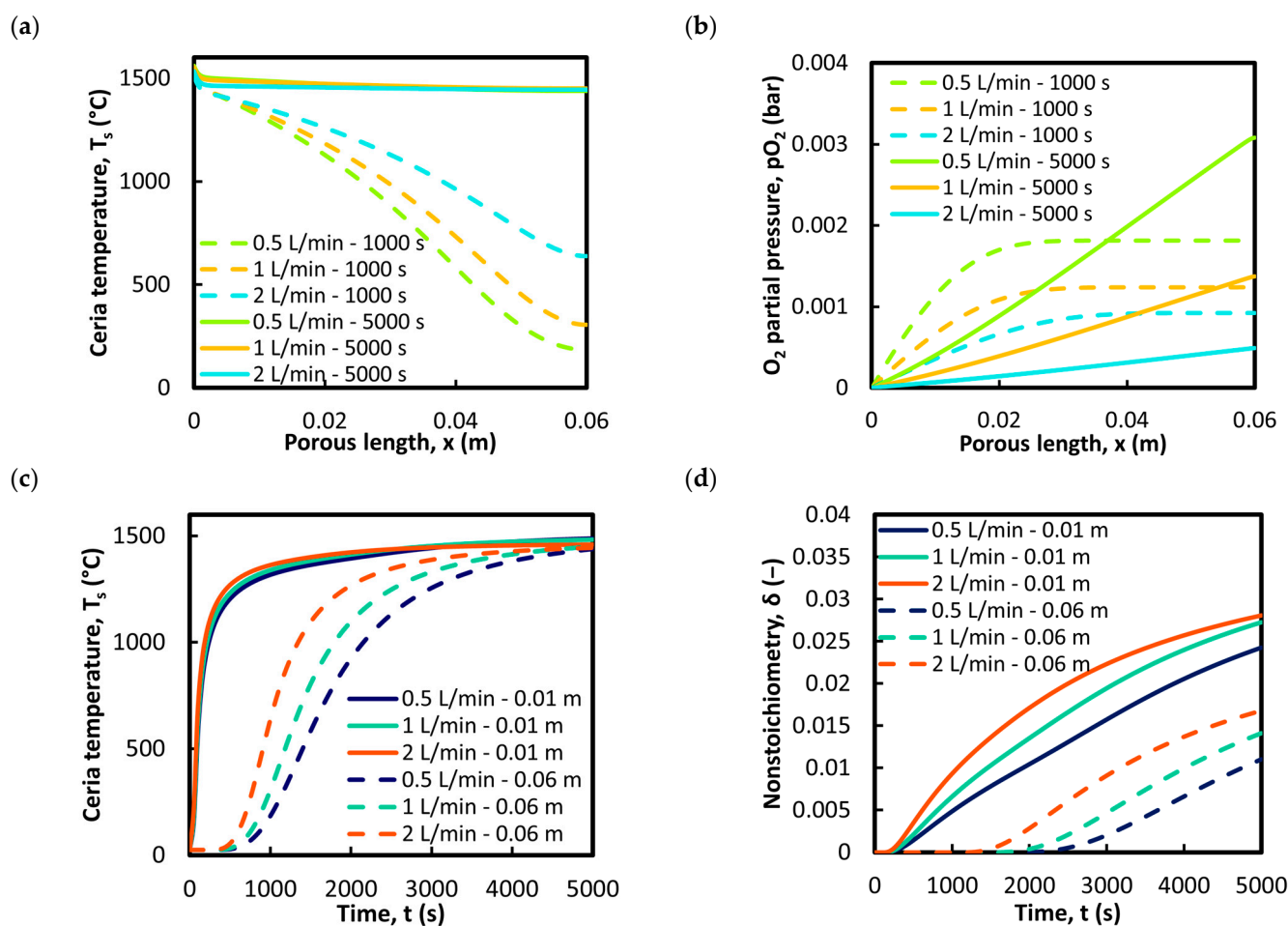


Figure 6. Effect of the N₂ (sweeping gas) volumetric flow rate during the reduction step of the first cycle. (a) Ceria (solid phase) temperature and (b) O₂ partial pressure in space at 1000 s and 5000 s. (c) Ceria (solid phase) temperature and (d) nonstoichiometry in time at 0.01 m and 0.06 m (outlet) from the inlet.

3.3.2. Steam Concentration During Oxidation

The impact of the variation in the molar concentration of steam in the oxidation feed was verified in the range of 0.2–0.4, which was the experimental range in which the kinetic law was derived [59]. The outcomes from the reduction with 1 L/min of sweeping gas were taken as the initial values. The results are coherent with the expectations and further confirm the robustness of the approach for the implementation of kinetics. Figure 7a shows the solid conversion in space, with a consistent improvement when increasing H₂O content in the feed, which was especially highlighted after 90 s (after the production peak). The hydrogen production peak in time is depicted in Figure 7b, with faster hydrogen production and reaction completion for higher oxidant concentrations. The production peak value fell at earlier times as the kinetics became faster, anticipating the time of maximum H₂O feeding (60 s) when looking at the 40% concentration profile. However, pure steam would be typically fed in a real system, leading, in principle, to faster kinetics and, thus, to a more efficient operation [45]. For completeness, Figure 7b also reports a reference to the H₂ production rate profile as obtained from a 100% steam input simulation.

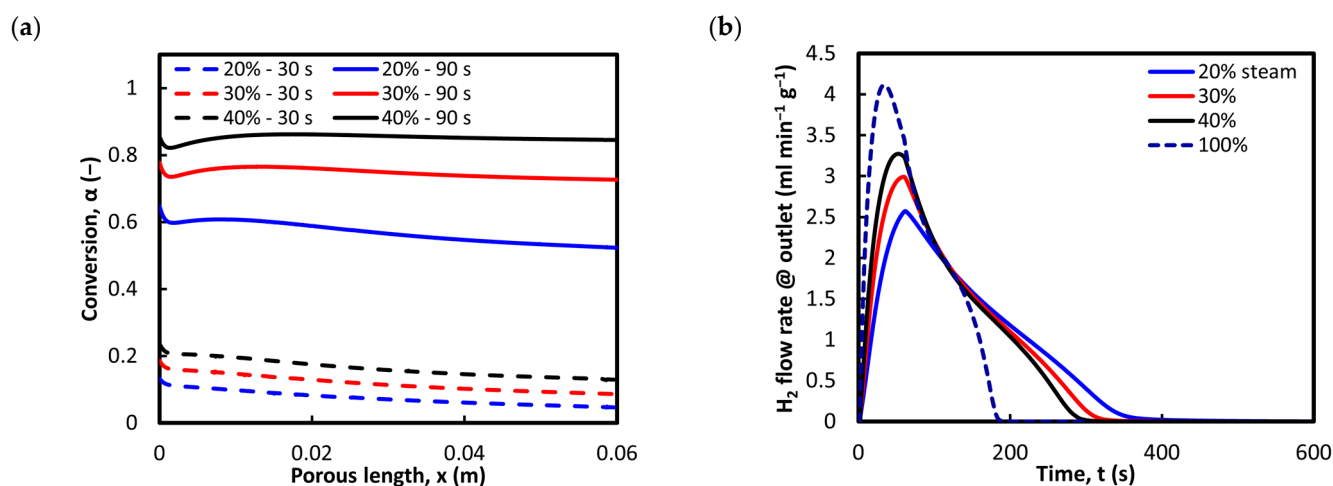


Figure 7. Effect of the H₂O concentration during the oxidation step of the first cycle, considering 20%, 30%, and 40% molar fractions. (a) Conversion at 30 s and 90 s from the beginning of the oxidation step. (b) Outlet hydrogen volumetric flow rate in time, also including the production profile obtained with 100% steam input.

3.4. Verification of the Redox Model

The robustness of the redox kinetic model is verified by looking at the oxygen mass balance during the reduction step (oxygen release) and the following oxidation step (oxygen uptake) of the first redox cycle. This is accomplished directly by computing the net oxygen and hydrogen sources across the entire computational domain through integration in time and space (Equations (37) and (38)).

$$n_{\text{O}} = \int_0^{t_{\text{red}}} \int_0^{L_{\text{OC}}} \frac{2A_{\text{OC}}}{M_{\text{O}_2}} R_{\text{O}_2} dx dt \quad (37)$$

$$n_{\text{H}_2} = \int_0^{t_{\text{ox}}} \int_0^{L_{\text{OC}}} \frac{A_{\text{OC}}}{M_{\text{H}_2}} R_{\text{H}_2} dx dt \quad (38)$$

Figure 8a shows the redox mass balance in all the parametric conditions investigated, confirming that the hydrogen produced during the oxidation step nearly matches the full replenishment of the oxygen released during the previous reduction, with a reoxidation extent higher than 0.985 in all the operating conditions (Figure 8b). The minimal difference would asymptotically disappear when running the oxidation step for arbitrarily longer

times. The hydrogen produced increases at higher steam concentrations with a fixed sweeping flow rate during reduction, but this dependence is relatively less relevant here since 600 s was sufficient to fully reoxidize the ceria in all the flow conditions studied. On the other hand, the hydrogen production dependence was stronger with the increasing sweeping flow rate, corresponding to the higher oxygen vacancies that were produced during the previous reduction.

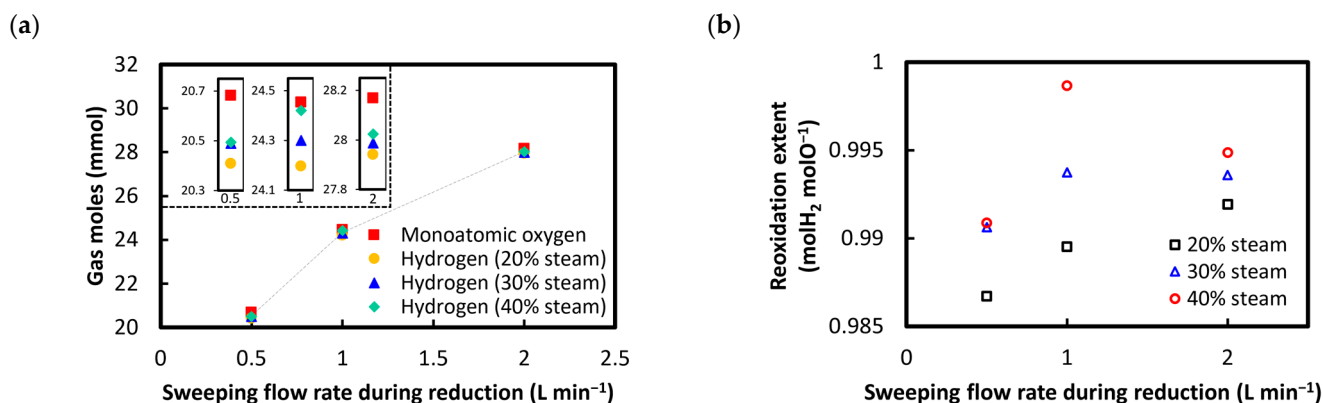


Figure 8. Oxygen mass balance across the redox cycle as a function of the reduction flow rate and steam content in the oxidation feed. (a) Gas moles (monoatomic oxygen released during reduction, red markers; molecular hydrogen produced during oxidation, other coloured markers) exchanged during the redox cycle. The top-left inset shows the zoomed-in points. (b) Reoxidation extent (moles of molecular hydrogen produced per mole of monoatomic oxygen released).

3.5. Multiple Cycling

Three consecutive cycles were simulated in the flow conditions that ensured the highest gas evolution volumes, i.e., reduction with a 2 L/min sweeping flow rate and oxidation at 40% of the H₂O molar concentration. The first cycle duration was kept at a 5000 s long reduction and a 600 s long oxidation, whereas the following cycles were simulated with shorter durations (an 1800 s long reduction and 300 s long oxidation). Figure 9 depicts the monoatomic oxygen and hydrogen reaction rates as integral quantities in the entire domain, along with the nonstoichiometry in two different points of the domain—at the inlet and at 1 cm from the inlet. The system reached a steady state from the second cycle onwards. Overall, the redox analytical model can, thus, be used for modelling long cyclic operations to foresee the long-duration performance of the simulated system under investigation.

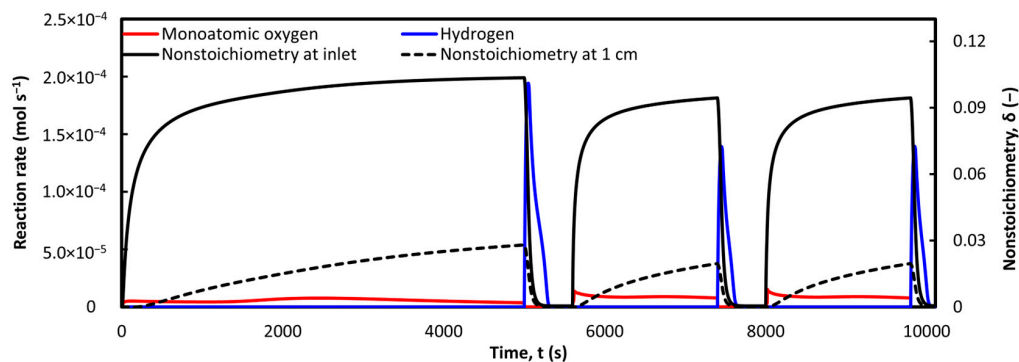


Figure 9. Nonstoichiometry and reaction rate results from the simulation of three consecutive redox cycles.

4. Model Applications

The simple analytical approach developed in this work should be helpful in reactor-level modelling, where the redox kinetics must be coupled with heat transfer and fluid flow. The usefulness of the methodology is summarized below.

- i. The analytical model makes use of global (or apparent) kinetic laws that can be obtained experimentally from thermogravimetry or online gas analysis. Typically, a solid-state rate equation of this type is expressed in the following form [39,59], as also described in more detail in Section 2.4.2:

$$\frac{d\alpha}{dt} = k(T)f(\alpha)h(x_i) \quad (39)$$

The solid conversion variation in time, thus, results from the factorized contributions of the reaction temperature, T , of the solid conversion itself, α , and of the gas atmosphere through the reactants' partial pressure or molar fraction, x . Extensive literature is available on this type of kinetic study [39], and a considerable number of previous works have addressed the definition of this kind of kinetic law in chemical looping redox cycles and with different oxygen carriers (OCs), such as H_2 -assisted Fe_3O_4 reduction in FeO/Fe [78], the isothermal reverse water–gas shift chemical looping of $Fe_2O_3-Ce_{0.5}Zr_{0.5}O_2$ [79], H_2 -assisted reduction in the Fe_3O_4/ZrO_2 composite [80], CH_4 -assisted reduction in Fe_3O_4 [81], and CH_4 -assisted reduction in nonstoichiometric $LaFeO_3$ [82]. Most interestingly, the ceria redox cycle was studied with this approach [13], with relevant examples for the CO_2 [51] and H_2O splitting step [59]. The usefulness of extracting a complete kinetics law lies in its potential use in modelling reactor systems and simulating the process behaviour. However, apparent kinetic laws are obtained from experiments as a bulk measurement of the tested sample. This aspect is highlighted in a recent review on solar thermochemical reaction systems modelling [27]: “The use of this experimental data directly in a continuum model [...] requires some care since this is a bulk solid measurement that must be related to local gas/solid concentrations”. Our analytical model meets this gap, allowing the conversion of global kinetic law into a local kinetic law, which can be readily coupled to other physics in reactor-level numerical modelling. The simple method consists of expressing the solid conversion α as a function of the nonstoichiometry δ of the OC instead of as a function of the sample mass, thereby addressing a local dependence instead of a global bulk dependence. This allows $\frac{\partial \alpha}{\partial t}$ to correlate with $\frac{\partial \delta}{\partial t}$ via differentiation and eventually express the chemical species mass source/sink, R_i , in terms of the local fields (e.g., temperature and species concentrations).

- ii. The approach developed fits any nonstoichiometric oxide, which can be used as the OC in any chemical looping redox cycle for synthetic fuel production. Indeed, the equations derived herein for the H_2O -driven oxidation of ceria can be adapted to CO_2 -driven oxidation and to fuel-assisted reduction reactions (such as in the reverse water–gas shift H_2 -assisted process [83] or in the methane reforming process [84]) through the reactant concentration-dependent term, as well as to thermal reduction reactions. Despite sparse examples in the literature [56], to the best of our knowledge, this is the first time that an analytical approach has been rigorously derived for the use of apparent kinetics in (solar) reactor continuum-level modelling and applied to thermochemical fuel production. Robust validation against experimental data secures the validity of our methodology.

- iii. In this work, a kinetic law taking into account only the forward reaction was considered, according to Arifin et al. [59]. Details are given in Section 2.4.2. As mentioned, this form of the rate equation is valid given that the reaction products can be removed in a sufficiently fast way, such as to prevent a backward reaction. Equivalently, this happens when a large excess of the gaseous reactant is supplied to the reaction site [39]. When dealing with thermochemical splitting, this condition is typically met when using perovskite OCs, which have shown a higher reduction extent and lower reduction temperatures than ceria but a lower reoxidation extent at the same time unless the oxidant in excess is used to boost the thermodynamic driving force [7,15]. Thus, according to these considerations, the form of the model presented in this work could match the kinetic rate equation form well and is usually suitable for perovskite OCs. In addition, the large steam excess needed by perovskite OCs calls for necessity of optimizing the oxidation step in terms of fluid flow, kinetics, and reaction times. This can be addressed using our methodology and suitable rate expressions for the OC under investigation. However, it should be kept in mind that ignoring the backward reaction still represents an approximation with respect to the real process, and previous works have highlighted this behaviour [85]. This means that the proposed model could be improved in the future, including the backward kinetics in the overall chemistry modelling. Nonetheless, we can reasonably assert that the assumption considered here gains increasing accuracy when kinetics can be considered slow with respect to the reactant's advection.
- iv. Being based on a local approach, our analytical model is dimensionally independent. Thus, it can be applied to any (solar) reactor geometry and can be useful to model much more complex systems than the one simulated herein, up to complete 2D/3D models. The inherently local nature of the model also allows spatial distributions of the redox material conversion/utilization and its reactivity in time to be obtained, paving the way for optimization strategies of the reactor's design and operation.

5. Conclusions

In this work, we develop a novel, simple analytical approach for converting global (or apparent) kinetic laws into local kinetic laws, thereby allowing their ready implementation into numerical modelling at the continuum reactor level. This type of kinetics treatment is often addressed to describe a large variety of reactions in the field of chemical looping and solar thermochemical processes, but a rigorous analytical methodology for the use of such kinetics is missing. The implementation of the approach developed was exemplified in the ceria-based thermochemical redox cycle, specifically in the H₂O-driven oxidation step, during which solar thermochemical hydrogen was produced. While the thermal reduction kinetics were implemented according to well-established rate models, the H₂ production rate equation was derived, rearranging apparent kinetics from the literature into a more suitable analytical form that could be readily implemented into multiphysics reactor models using our proposed methodology against previous models simulating the oxidation either at thermodynamic equilibrium or with alternative approaches for the kinetics treatment. Simulated O₂ production rate profiles during reduction and H₂ production rate profiles during oxidation were compared with experimental data from the literature showing high agreement, thereby validating the numerical implementation. The multiphysics model simulates the entire redox cycle in a simplified 1D geometry and includes the coupling among heat transfer, fluid flow, and redox chemistry, describing a directly irradiated solar receiver–reactor and making use of simplifying assumptions for the radiation. The robustness of the model is secured via the oxygen mass balance across the redox cycle. The analytical approach is thought to be useful for simulating any nonstoichiometric oxide

in chemical looping synthetic fuel production cycles of various nature, such as the ceria system and, most notably, perovskites, these latter typically requiring large amounts of excess steam during oxidation. Recently, Li et al. [7] developed a thermodynamic model for the analysis of both state-of-the-art and hypothetical materials, demonstrating how perovskites are extremely difficult to reoxidize and how their high fuel outputs are achieved at the cost of huge water-heating requirements, causing extremely low efficiencies. This latter consideration implies that fluid flow, redox kinetics, and reaction times should be thoroughly modelled and optimized when dealing with oxidation-critical OCs, such as perovskites. The importance of modelling the oxidation kinetics was also underlined by de la Calle et al. [55] since the thermodynamic modelling of the process—although relevant for fixing the upper limits in the efficiency—only represents the ideal boundaries of the process operation. It is, thus, of utmost relevance to develop efficient methods to readily simulate the redox kinetics of any nonstoichiometric redox material together with the complex process of multiphysics. Nonstoichiometric OCs are indeed reported as the most explored class of OCs at present [3]. Moreover, being based on a local approach, our analytical model can be readily applied to arbitrarily complex reactor geometries. The inherently local nature of the model also allows the spatial distributions of the redox material conversion/its utilization to be obtained in time, paving the way for optimization strategies of the reactor’s design and operation. Finally, a literature overview of selected numerical modelling works on solar reactor systems was provided.

Future developments will include multiphysics modelling at higher dimensionality (2D+ models), applying our novel methodology. A further comparison against equilibrium models will quantitatively predict the necessity of taking the reaction kinetics into account. The detailed calibration of the rate equation coupled with advanced OC morphologies [35] will also be addressed, together with more accurate assumptions for the pO_2 field through the porous medium, as well as for radiative heat transfer. The use of our comprehensive model for optimizing the reactor design and operation, in terms of uniform utilization and the conversion of the OC, will also be shown.

Author Contributions: Conceptualization, F.O.; methodology, F.O.; validation, F.O.; formal analysis, F.O.; investigation, F.O.; resources, D.F. and M.S.; data curation, F.O.; writing—original draft preparation, F.O.; writing—review and editing, D.F., D.P. and M.S.; visualization, F.O.; supervision, D.F., D.P. and M.S. All authors have read and agreed to the published version of the manuscript.

Funding: This research received no external funding.

Data Availability Statement: The original contributions presented in the study are included in the article, further inquiries can be directed to the corresponding author.

Conflicts of Interest: The authors declare no conflicts of interest.

Nomenclature

Acronyms

LTE	Local Thermal Equilibrium
LTNE	Local Thermal Non-Equilibrium
RDA	Rosseland Diffusion Approximation
RPC	Reticulated Porous Ceramics
OC	Oxygen carrier

Greek Symbols

α	Solid conversion, 1
β_R	Rosseland mean extinction coefficient, m^{-1}
γ	Concentration exponent, 1

δ	Nonstoichiometry, 1
δ_{\max}	Maximum nonstoichiometry, 1
ε	Macro-scale porosity, 1
ρ	Density, kg m^{-3}
σ	Stefan–Boltzmann constant, $\text{W m}^{-2}\text{K}^{-4}$
σ_{ij}	Characteristic length, \AA
Λ	Proportionality constant, kg m^{-3}
μ	Dynamic viscosity, Pa s
ω	Mass fraction, 1
Ω_{D}	Diffusion collision integral, 1
Subscripts	
0	Initial time
c	Chemical
f	Fluid
i	ith chemical species
ox	Oxidation
r	Radiation
red	Reduction
s	Solid
∞	Thermodynamic equilibrium
Symbols	
A_{OC}	Exposed (irradiated) area, m^2
A_{sf}	Specific surface area, m^{-1}
A	Preexponential factor, s^{-1}
c_p	Heat capacity at constant pressure, $\text{kg}^{-1}\text{K}^{-1}$
d_m	Mean pore diameter, m
D^f	Diffusion coefficient, $\text{m}^2 \text{s}^{-1}$
D_{OC}	Diameter of the exposed (irradiated) area, m
E	Activation energy, kJ mol^{-1}
f	Differential mechanistic model, 1
F	Forchheimer coefficient, m^{-1}
$\Delta h_{\text{H}_2\text{O,diss}}$	Water dissociation reaction enthalpy, J mol^{-1}
Δh_{red}	Oxygen vacancy formation enthalpy, J mol^{-1}
h_{sf}	Heat transfer coefficient, $\text{W m}^{-2}\text{K}^{-1}$
h	Concentration dependent function, 1
j	Diffusive flux, $\text{kg m}^{-2}\text{s}^{-1}$
k	Rate constant, s^{-1}
k_f	Thermal conductivity of the fluid phase, $\text{W m}^{-1}\text{K}^{-1}$
k_s	Thermal conductivity of the solid phase, $\text{W m}^{-1}\text{K}^{-1}$
K	Permeability, m^2
L_{OC}	Thickness of the porous medium, m
M	Molar mass, kg mol^{-1}
n	Number of moles, mol
n_{O_2}	O_2 partial pressure exponent, 1
Nu	Nusselt number, 1
p	Pressure, Pa or bar
Pr	Prandtl number, 1
\dot{q}	Thermal power source or sink, W m^{-3}
R_g	Gas constant, $\text{J mol}^{-1}\text{K}^{-1}$
R	Mass source, $\text{kg m}^{-3}\text{s}^{-1}$
Re	Reynolds number, 1
T	Temperature, K
u	Darcy velocity vector, m s^{-1}
x	Molar fraction, 1, or spatial coordinate, m

References

1. Wei, L.; Pan, Z.; Shi, X.; Esan, O.C.; Li, G.; Qi, H.; Wu, Q.; An, L. Solar-driven thermochemical conversion of H₂O and CO₂ into sustainable fuels. *iScience* **2023**, *26*, 108127. [[CrossRef](#)]
2. Jeje, S.O.; Marazani, T.; Obiko, J.O.; Shongwe, M.B. Advancing the hydrogen production economy: A comprehensive review of technologies, sustainability, and future prospects. *Int. J. Hydrogen Energy* **2024**, *78*, 642–661. [[CrossRef](#)]
3. Tran, J.T.; Warren, K.J.; Wilson, S.A.; Muhich, C.L.; Musgrave, C.B.; Weimer, A.W. An updated review and perspective on efficient hydrogen generation via solar thermal water splitting. *WIREs Energy Environ.* **2024**, *13*, e528. [[CrossRef](#)]
4. Schächli, R.; Hüsler, V.; Steinfeld, A. Solar Thermochemical Production of Syngas from H₂O and CO₂—Experimental Parametric Study, Control, and Automation. *Ind. Eng. Chem. Res.* **2024**, *63*, 3563–3575. [[CrossRef](#)]
5. Schächli, R.; Rutz, D.; Dähler, F.; Muroyama, A.; Haueter, P.; Lilliestam, J.; Patt, A.; Furler, P.; Steinfeld, A. Drop-in fuels from sunlight and air. *Nature* **2022**, *601*, 63–68. [[CrossRef](#)] [[PubMed](#)]
6. Chang, W.; Hu, Y.; Xu, W.; Huang, C.; Chen, H.; He, J.; Han, Y.; Zhu, Y.; Ma, X.; Wang, X. Recent Advances of Oxygen Carriers for Hydrogen Production via Chemical Looping Water-Splitting. *Catalysts* **2023**, *13*, 279. [[CrossRef](#)]
7. Li, S.; Wheeler, V.M.; Kumar, A.; Venkataraman, M.B.; Muhich, C.L.; Hao, Y.; Lipiński, W. Thermodynamic Guiding Principles for Designing Nonstoichiometric Redox Materials for Solar Thermochemical Fuel Production: Ceria, Perovskites, and Beyond. *Energy Technol.* **2022**, *10*, 2000925. [[CrossRef](#)]
8. Coronado, J.M.; Bayón, A. Catalytic enhancement of production of solar thermochemical fuels: Opportunities and limitations. *Phys. Chem. Chem. Phys.* **2023**, *25*, 17092–17106. [[CrossRef](#)]
9. Lou, J.; Tian, Z.; Wu, Y.; Li, X.; Qian, X.; Haile, S.M.; Hao, Y. Thermodynamic assessment of nonstoichiometric oxides for solar thermochemical fuel production. *Sol. Energy* **2022**, *241*, 504–514. [[CrossRef](#)]
10. Joshi, A.; Shah, V.; Mohapatra, P.; Kumar, S.; Joshi, R.K.; Kathe, M.; Qin, L.; Tong, A.; Fan, L.-S. Chemical looping—A perspective on the next-gen technology for efficient fossil fuel utilization. *Adv. Appl. Energy* **2021**, *3*, 100044. [[CrossRef](#)]
11. Kim, Y.; Lim, H.S.; Kim, H.S.; Lee, M.; Lee, J.W.; Kang, D. Carbon dioxide splitting and hydrogen production using a chemical looping concept: A review. *J. CO₂ Util.* **2022**, *63*, 102139. [[CrossRef](#)]
12. Al-Gamal, A.G.; Yehia, F.; Elmasry, M.R.; El-Khair, M.A.A.; Kandeel, H.S.; Elseman, A.M.; Kim, D.-H.; Kabel, K.I. Perovskite materials for hydrogen evolution: Processes, challenges and future perspectives. *Int. J. Hydrogen Energy* **2024**, *79*, 1113–1138. [[CrossRef](#)]
13. Lu, Y.; Zhu, L.; Agrafiotis, C.; Vieten, J.; Roeb, M.; Sattler, C. Solar fuels production: Two-step thermochemical cycles with cerium-based oxides. *Prog. Energy Combust. Sci.* **2019**, *75*, 100785. [[CrossRef](#)]
14. Boretti, A. Technology Readiness Level of Solar Thermochemical Splitting Cycles. *ACS Energy Lett.* **2021**, *6*, 1170–1174. [[CrossRef](#)]
15. Carrillo, R.J.; Scheffe, J.R. Advances and trends in redox materials for solar thermochemical fuel production. *Sol. Energy* **2017**, *156*, 3–20. [[CrossRef](#)]
16. Scheffe, J.R.; Steinfeld, A. Oxygen exchange materials for solar thermochemical splitting of H₂O and CO₂: A review. *Mater. Today* **2014**, *17*, 341–348. [[CrossRef](#)]
17. Lidor, A.; Bulfin, B. A critical perspective and analysis of two-step thermochemical fuel production cycles. *Sol. Compass* **2024**, *11*, 100077. [[CrossRef](#)]
18. Mao, Y.; Gao, Y.; Dong, W.; Wu, H.; Song, Z.; Zhao, X.; Sun, J.; Wang, W. Hydrogen production via a two-step water splitting thermochemical cycle based on metal oxide—A review. *Appl. Energy* **2020**, *267*, 114860. [[CrossRef](#)]
19. Weber, A.; Grobbel, J.; Puttkamer, M.N.-V.; Sattler, C. Swept open moving particle reactor including heat recovery for solar thermochemical fuel production. *Sol. Energy* **2023**, *266*, 112178. [[CrossRef](#)]
20. Brendelberger, S.; Holzemer-Zerhusen, P.; Puga, E.V.; Roeb, M.; Sattler, C. Study of a new receiver-reactor cavity system with multiple mobile redox units for solar thermochemical water splitting. *Sol. Energy* **2022**, *235*, 118–128. [[CrossRef](#)]
21. Puga, E.V.; Brendelberger, S.; Weber, A.; Sattler, C. Modelling Development of a Receiver-Reactor of Type R2Mx for Thermochemical Water Splitting. In Proceedings of the ASME 2023 17th International Conference on Energy Sustainability Collocated with the ASME 2023 Heat Transfer Summer Conference, Washington DC, USA, 10–12 July 2023; American Society of Mechanical Engineers Digital Collection. American Society of Mechanical Engineers: New York, NY, USA, 2023. [[CrossRef](#)]
22. Patankar, A.S.; Wu, X.-Y.; Choi, W.; Tuller, H.L.; Ghoniem, A.F. A Reactor Train System for Efficient Solar Thermochemical Fuel Production. *J. Sol. Energy Eng.* **2022**, *144*, 061014. [[CrossRef](#)]
23. Gokon, N.; Takahashi, S.; Yamamoto, H.; Kodama, T. New Solar Water-Splitting Reactor with Ferrite Particles in an Internally Circulating Fluidized Bed. *J. Sol. Energy Eng.* **2009**, *131*, 011007. [[CrossRef](#)]
24. Tran, J.T.; Warren, K.J.; Wilson, C.; Taylor, L.; Anderson, R.L.; Mejjic, D.; Weimer, A.W. Feasibility of continuous water and carbon dioxide splitting via a pressure-swing, isothermal redox cycle using iron aluminates. *Chem. Eng. J.* **2024**, *497*, 154791. [[CrossRef](#)]
25. Zoller, S.; Koepf, E.; Nizamian, D.; Stephan, M.; Patané, A.; Haueter, P.; Romero, M.; González-Aguilar, J.; Lieftink, D.; de Wit, E.; et al. A solar tower fuel plant for the thermochemical production of kerosene from H₂O and CO₂. *Joule* **2022**, *6*, 1606–1616. [[CrossRef](#)]
26. Marxer, D.; Furler, P.; Takacs, M.; Steinfeld, A. Solar thermochemical splitting of CO₂ into separate streams of CO and O₂ with high selectivity, stability, conversion, and efficiency. *Energy Environ. Sci.* **2017**, *10*, 1142–1149. [[CrossRef](#)]

27. Wheeler, V.M.; Bader, R.; Kreider, P.B.; Hangi, M.; Haussener, S.; Lipiński, W. Modelling of solar thermochemical reaction systems. *Sol. Energy* **2017**, *156*, 149–168. [[CrossRef](#)]
28. Keene, D.J.; Davidson, J.H.; Lipiński, W. A Model of Transient Heat and Mass Transfer in a Heterogeneous Medium of Ceria Undergoing Nonstoichiometric Reduction. *J. Heat Transf.* **2013**, *135*, 052701. [[CrossRef](#)]
29. Keene, D.J.; Lipiński, W.; Davidson, J.H. The effects of morphology on the thermal reduction of nonstoichiometric ceria. *Chem. Eng. Sci.* **2014**, *111*, 231–243. [[CrossRef](#)]
30. Chandran, R.B.; Bader, R.; Lipiński, W. Transient heat and mass transfer analysis in a porous ceria structure of a novel solar redox reactor. *Int. J. Therm. Sci.* **2015**, *92*, 138–149. [[CrossRef](#)]
31. Lidor, A.; Fend, T.; Roeb, M.; Sattler, C. Parametric investigation of a volumetric solar receiver-reactor. *Sol. Energy* **2020**, *204*, 256–269. [[CrossRef](#)]
32. Furler, P.; Steinfeld, A. Heat transfer and fluid flow analysis of a 4 kW solar thermochemical reactor for ceria redox cycling. *Chem. Eng. Sci.* **2015**, *137*, 373–383. [[CrossRef](#)]
33. Zoller, S.; Koepf, E.; Roos, P.; Steinfeld, A. Heat Transfer Model of a 50 kW Solar Receiver-Reactor for Thermochemical Redox Cycling Using Cerium Dioxide. *J. Sol. Energy Eng.* **2019**, *141*, 021014. [[CrossRef](#)]
34. Sharma, J.P.; Kumar, R.; Ahmadi, M.H.; Mukhtar, A.; Yasir, A.S.H.M.; Sharifpur, M.; Ongar, B.; Yegzekova, A. Chemical and thermal performance analysis of a solar thermochemical reactor for hydrogen production via two-step WS cycle. *Energy Rep.* **2023**, *10*, 99–113. [[CrossRef](#)]
35. Li, S.; Wheeler, V.M.; Kumar, A.; Lipiński, W. Numerical modelling of ceria undergoing reduction in a particle-gas counter-flow: Effects of chemical kinetics under isothermal conditions. *Chem. Eng. Sci.* **2020**, *218*, 115553. [[CrossRef](#)]
36. Zhang, H.; Smith, J.D. Investigating influences of geometric factors on a solar thermochemical reactor for two-step carbon dioxide splitting via CFD models. *Sol. Energy* **2019**, *188*, 935–950. [[CrossRef](#)]
37. Ma, T.; Fu, M.; Cong, J.; Zhang, X.; Zhang, Q.; Sayfieva, K.F.; Chang, Z.; Li, X. Analysis of heat and mass transfer in a porous solar thermochemical reactor. *Energy* **2024**, *294*, 130842. [[CrossRef](#)]
38. Li, L.; Chen, C.; Singh, A.; Rahmatian, N.; AuYeung, N.; Randhir, K.; Mei, R.; Klausner, J.F.; Hahn, D.W.; Petrasch, J. A transient heat transfer model for high temperature solar thermochemical reactors. *Int. J. Hydrogen Energy* **2016**, *41*, 2307–2325. [[CrossRef](#)]
39. Vyazovkin, S.; Burnham, A.K.; Criado, J.M.; Pérez-Maqueda, L.A.; Popescu, C.; Sbirrazzuoli, N. ICTAC Kinetics Committee recommendations for performing kinetic computations on thermal analysis data. *Thermochim. Acta* **2011**, *520*, 1–19. [[CrossRef](#)]
40. Bulfin, B.; Lowe, A.J.; Keogh, K.A.; Murphy, B.E.; Lübben, O.; Krasnikov, S.A.; Shvets, I.V. Analytical Model of CeO₂ Oxidation and Reduction. *J. Phys. Chem. C* **2013**, *117*, 24129–24137. [[CrossRef](#)]
41. Ishida, T.; Gokon, N.; Hatamachi, T.; Kodama, T. Kinetics of Thermal Reduction Step of Thermochemical Two-Step Water Splitting Using CeO₂ Particles: MASTER-Plot Method for Analyzing Non-Isothermal Experiments. *Energy Procedia* **2014**, *49*, 1970–1979. [[CrossRef](#)]
42. Lapp, J.; Davidson, J.H.; Lipiński, W. Heat Transfer Analysis of a Solid-Solid Heat Recuperation System for Solar-Driven Nonstoichiometric Redox Cycles. *J. Sol. Energy Eng.* **2013**, *135*, 031004. [[CrossRef](#)]
43. Bader, R.; Chandran, R.B.; Venstrom, L.J.; Sedler, S.J.; Krenzke, P.T.; De Smith, R.M.; Banerjee, A.; Chase, T.R.; Davidson, J.H.; Lipiński, W. Design of a Solar Reactor to Split CO₂ via Isothermal Redox Cycling of Ceria. *J. Sol. Energy Eng.* **2015**, *137*, 031007. [[CrossRef](#)]
44. Huang, H.; Lin, M. Optimization of solar receivers for high-temperature solar conversion processes: Direct vs. Indirect illumination designs. *Appl. Energy* **2021**, *304*, 117675. [[CrossRef](#)]
45. Lidor, A.; Fend, T.; Roeb, M.; Sattler, C. High performance solar receiver-reactor for hydrogen generation. *Renew. Energy* **2021**, *179*, 1217–1232. [[CrossRef](#)]
46. Lapp, J.; Lipiński, W. Transient Three-Dimensional Heat Transfer Model of a Solar Thermochemical Reactor for H₂O and CO₂ Splitting via Nonstoichiometric Ceria Redox Cycling. *J. Sol. Energy Eng.* **2014**, *136*, 031006. [[CrossRef](#)]
47. Venstrom, L.J.; De Smith, R.M.; Chandran, R.B.; Boman, D.B.; Krenzke, P.T.; Davidson, J.H. Applicability of an Equilibrium Model to Predict the Conversion of CO₂ to CO via the Reduction and Oxidation of a Fixed Bed of Cerium Dioxide. *Energy Fuels* **2015**, *29*, 8168–8177. [[CrossRef](#)]
48. Chandran, R.B.; Davidson, J.H. Model of transport and chemical kinetics in a solar thermochemical reactor to split carbon dioxide. *Chem. Eng. Sci.* **2016**, *146*, 302–315. [[CrossRef](#)]
49. Pan, H.; Lu, Y.; Zhu, L. Numerical Modeling of CO₂ Splitting in High-Temperature Solar-Driven Oxygen Permeation Membrane Reactors. *J. Sol. Energy Eng.* **2021**, *143*, 021001. [[CrossRef](#)]
50. Le Gal, A.; Abanades, S.; Flamant, G. CO₂ and H₂O Splitting for Thermochemical Production of Solar Fuels Using Nonstoichiometric Ceria and Ceria/Zirconia Solid Solutions. *Energy Fuels* **2011**, *25*, 4836–4845. [[CrossRef](#)]
51. Farooqui, A.; Pica, A.M.; Marocco, P.; Ferrero, D.; Lanzini, A.; Fiorilli, S.; Llorca, J.; Santarelli, M. Assessment of kinetic model for ceria oxidation for chemical-looping CO₂ dissociation. *Chem. Eng. J.* **2018**, *346*, 171–181. [[CrossRef](#)]
52. Wang, P.; Wei, R.K.; Vafai, K. A dual-scale transport model of the porous ceria based on solar thermochemical cycle water splitting hydrogen production. *Energy Convers. Manag.* **2022**, *272*, 116363. [[CrossRef](#)]

53. Zhao, Z.; Uddi, M.; Tsvetkov, N.; Yildiz, B.; Ghoniem, A.F. Redox Kinetics Study of Fuel Reduced Ceria for Chemical-Looping Water Splitting. *J. Phys. Chem. C* **2016**, *120*, 16271–16289. [[CrossRef](#)]
54. Dai, X.; Haussener, S. Non-Uniform Porous Structures and Cycling Control for Optimized Fixed-Bed Solar Thermochemical Water Splitting. *J. Sol. Energy Eng.* **2022**, *144*, 030904. [[CrossRef](#)]
55. de la Calle, A.; Ermanoski, I.; Miller, J.E.; Stechel, E.B. Towards chemical equilibrium in thermochemical water splitting. Part 2: Re-oxidation. *Int. J. Hydrogen Energy* **2024**, *72*, 1159–1168. [[CrossRef](#)]
56. Wang, B.; Li, L.; Schäfer, F.; Pottas, J.J.; Kumar, A.; Wheeler, V.M.; Lipiński, W. Thermal reduction of iron–manganese oxide particles in a high-temperature packed-bed solar thermochemical reactor. *Chem. Eng. J.* **2021**, *412*, 128255. [[CrossRef](#)]
57. Wei, L.; Li, Z.; Pan, Z.; Yi, Z.; Li, G.; An, L. A design of solar-driven thermochemical reactor integrated with heat recovery for continuous production of renewable fuels. *Energy Convers. Manag.* **2024**, *310*, 118484. [[CrossRef](#)]
58. Lougou, B.G.; Shuai, Y.; Pan, R.; Chaffa, G.; Tan, H. Heat transfer and fluid flow analysis of porous medium solar thermochemical reactor with quartz glass cover. *Int. J. Heat Mass Transf.* **2018**, *127*, 61–74. [[CrossRef](#)]
59. Arifin, D.; Weimer, A.W. Kinetics and mechanism of solar-thermochemical H₂ and CO production by oxidation of reduced CeO₂. *Sol. Energy* **2018**, *160*, 178–185. [[CrossRef](#)]
60. Lin, M.; Haussener, S. Solar fuel processing efficiency for ceria redox cycling using alternative oxygen partial pressure reduction methods. *Energy* **2015**, *88*, 667–679. [[CrossRef](#)]
61. Davenport, T.C.; Kemei, M.; Ignatowich, M.J.; Haile, S.M. Interplay of material thermodynamics and surface reaction rate on the kinetics of thermochemical hydrogen production. *Int. J. Hydrogen Energy* **2017**, *42*, 16932–16945. [[CrossRef](#)]
62. Le Gal, A.; Drobek, M.; Julbe, A.; Abanades, S. Improving solar fuel production performance from H₂O and CO₂ thermochemical dissociation using custom-made reticulated porous ceria. *Mater. Today Sustain.* **2023**, *24*, 100542. [[CrossRef](#)]
63. Bulfin, B.; Zuber, M.; Gräub, O.; Steinfeld, A. Intensification of the reverse water–gas shift process using a countercurrent chemical looping regenerative reactor. *Chem. Eng. J.* **2023**, *461*, 141896. [[CrossRef](#)]
64. Poling, B.E.; Prausnitz, J.M.; O’Connell, J.P. *The Properties Of Gases and Liquids*, 5th ed.; McGraw-Hill: New York, NY, USA, 2001.
65. Panlener, R.J. A thermodynamic study of nonstoichiometric cerium dioxide. *Journal of Physics and Chemistry of Solids* **1975**, *36*, 1213–1222. [[CrossRef](#)]
66. Panlener, R.; Blumenthal; Garnier, J. ICTAC Kinetics Committee recommendations for collecting experimental thermal analysis data for kinetic computations. *Thermochim. Acta* **2014**, *590*, 1–23. [[CrossRef](#)]
67. Bulfin, B.; Call, F.; Lange, M.; Lübben, O.; Sattler, C.; Pitz-Paal, R.; Shvets, I.V. Thermodynamics of CeO₂ Thermochemical Fuel Production. *Energy Fuels* **2015**, *29*, 1001–1009. [[CrossRef](#)]
68. Orsini, F.; Ferrero, D.; Cannone, S.F.; Santarelli, M.; Felli, A.; Boaro, M.; de Leitenburg, C.; Trovarelli, A.; Llorca, J.; Dimitrakopoulos, G.; et al. Exsolution-enhanced reverse water-gas shift chemical looping activity of Sr₂FeMo_{0.6}Ni_{0.4}O_{6-δ} double perovskite. *Chem. Eng. J.* **2023**, *475*, 146083. [[CrossRef](#)]
69. Marra, A.; Santarelli, M.; Papurello, D. Solar Dish Concentrator: A Case Study at the Energy Center Rooftop. *Int. J. Energy Res.* **2023**, *2023*, e9658091. [[CrossRef](#)]
70. NIST Chemistry WebBook. Available online: <https://webbook.nist.gov/chemistry/> (accessed on 22 April 2024).
71. Riess, I.; Ricken, M.; No, J. On the specific heat of nonstoichiometric ceria. *J. Solid State Chem.* **1985**, *57*, 314–322. [[CrossRef](#)]
72. Suter, S.; Steinfeld, A.; Haussener, S. Pore-level engineering of macroporous media for increased performance of solar-driven thermochemical fuel processing. *Int. J. Heat Mass Transf.* **2014**, *78*, 688–698. [[CrossRef](#)]
73. Brunser, S.S.; Bargardi, F.L.; Libanori, R.; Kaufmann, N.; Braun, H.; Steinfeld, A.; Studart, A.R. Solar-Driven Redox Splitting of CO₂ Using 3D-Printed Hierarchically Channeled Ceria Structures. *Adv. Mater. Interfaces* **2023**, *10*, 2300452. [[CrossRef](#)]
74. Petrasch, J.; Meier, F.; Friess, H.; Steinfeld, A. Tomography based determination of permeability, Dupuit–Forchheimer coefficient, and interfacial heat transfer coefficient in reticulate porous ceramics. *Int. J. Heat Fluid Flow* **2008**, *29*, 315–326. [[CrossRef](#)]
75. Mendes, M.A.A.; Talukdar, P.; Ray, S.; Trimis, D. Detailed and simplified models for evaluation of effective thermal conductivity of open-cell porous foams at high temperatures in presence of thermal radiation. *Int. J. Heat Mass Transf.* **2014**, *68*, 612–624. [[CrossRef](#)]
76. Loretz, M.; Maire, E.; Baillis, D. Analytical Modelling of the Radiative Properties of Metallic Foams: Contribution of X-ray Tomography. *Adv. Eng. Mater.* **2008**, *10*, 352–360. [[CrossRef](#)]
77. Bulfin, B.; Call, F.; Vieten, J.; Roeb, M.; Sattler, C.; Shvets, I.V. Oxidation and Reduction Reaction Kinetics of Mixed Cerium Zirconium Oxides. *J. Phys. Chem. C* **2016**, *120*, 2027–2035. [[CrossRef](#)]
78. Barde, A.A.; Klausner, J.F.; Mei, R. Solid state reaction kinetics of iron oxide reduction using hydrogen as a reducing agent. *Int. J. Hydrogen Energy* **2016**, *41*, 10103–10119. [[CrossRef](#)]
79. Wenzel, M.; Dharanipragada, N.A.; Galvita, V.V.; Poelman, H.; Marin, G.B.; Rihko-Struckmann, L.; Sundmacher, K. CO production from CO₂ via reverse water–gas shift reaction performed in a chemical looping mode: Kinetics on modified iron oxide. *J. CO₂ Util.* **2017**, *17*, 60–68. [[CrossRef](#)]
80. Tang, Q.; Ma, Y.; Huang, K. Fe₃O₄/ZrO₂ Composite as a Robust Chemical Looping Oxygen Carrier: A Kinetics Study on the Reduction Process. *ACS Appl. Energy Mater.* **2021**, *4*, 7091–7100. [[CrossRef](#)]

81. Lu, C.; Li, K.; Wang, H.; Zhu, X.; Wei, Y.; Zheng, M.; Zeng, C. Chemical looping reforming of methane using magnetite as oxygen carrier: Structure evolution and reduction kinetics. *Appl. Energy* **2018**, *211*, 1–14. [[CrossRef](#)]
82. Dai, X.; Cheng, J.; Li, Z.; Liu, M.; Ma, Y.; Zhang, X. Reduction kinetics of lanthanum ferrite perovskite for the production of synthesis gas by chemical-looping methane reforming. *Chem. Eng. Sci.* **2016**, *153*, 236–245. [[CrossRef](#)]
83. Wenzel, M. Reverse Water-Gas Shift Chemical Looping for Syngas Production from CO₂. Ph.D. Thesis, Otto-von-Guericke-Universität Magdeburg, Magdeburg, Germany, 2018. [[CrossRef](#)]
84. Krenzke, P.T.; Fosheim, J.R.; Davidson, J.H. Solar fuels via chemical-looping reforming. *Sol. Energy* **2017**, *156*, 48–72. [[CrossRef](#)]
85. Grobbel, J.; Sollich, M.F.; Quinto, D.M.; Lidor, A.; Sattler, C. Operation optimization of an array of receiver-reactors for solar fuel production. *AIP Conf. Proc.* **2022**, *2445*, 130004. [[CrossRef](#)]

Disclaimer/Publisher’s Note: The statements, opinions and data contained in all publications are solely those of the individual author(s) and contributor(s) and not of MDPI and/or the editor(s). MDPI and/or the editor(s) disclaim responsibility for any injury to people or property resulting from any ideas, methods, instructions or products referred to in the content.